

## MULTI-EPOCH VERY LONG BASELINE INTERFEROMETRIC OBSERVATIONS OF THE NUCLEAR STARBURST REGION OF NGC 253: IMPROVED MODELING OF THE SUPERNOVA AND STAR FORMATION RATES

H. RAMPADARATH<sup>1</sup>, J. S. MORGAN<sup>1</sup>, E. LENC<sup>2,3</sup>, AND S. J. TINGAY<sup>1</sup>

<sup>1</sup> International Centre for Radio Astronomy Research, Curtin University, GPO Box U1987, Perth, WA, Australia; hayden.rampadarath@icrar.org

<sup>2</sup> Sydney Institute for Astronomy, School of Physics, The University of Sydney, NSW, Australia

<sup>3</sup> ARC Centre of Excellence for All-sky Astrophysics (CAASTRO), Sydney, Australia

Received 2013 June 6; accepted 2013 October 29; published 2013 November 22

### ABSTRACT

The results of multi-epoch observations of the southern starburst galaxy, NGC 253, with the Australian Long Baseline Array at 2.3 GHz are presented. As with previous radio interferometric observations of this galaxy, no new sources were discovered. By combining the results of this survey with Very Large Array observations at higher frequencies from the literature, spectra were derived and a free-free absorption model was fitted of 20 known sources in NGC 253. The results were found to be consistent with previous studies. The supernova remnant, 5.48-43.3, was imaged with the highest sensitivity and resolution to date, revealing a two-lobed morphology. Comparisons with previous observations of similar resolution give an upper limit of  $10^4 \text{ km s}^{-1}$  for the expansion speed of this remnant. We derive a supernova rate of  $<0.2 \text{ yr}^{-1}$  for the inner 300 pc using a model that improves on previous methods by incorporating an improved radio supernova peak luminosity distribution and by making use of multi-wavelength radio data spanning 21 yr. A star formation rate of  $\text{SFR}(M \geq 5 M_{\odot}) < 4.9 M_{\odot} \text{ yr}^{-1}$  was also estimated using the standard relation between supernova and star formation rates. Our improved estimates of supernova and star formation rates are consistent with studies at other wavelengths. The results of our study point to the possible existence of a small population of undetected supernova remnants, suggesting a low rate of radio supernova production in NGC 253.

**Key words:** galaxies: individual (NGC 253) – galaxies: starburst – ISM: supernova remnants – radio continuum: galaxies – supernovae: general – techniques: interferometric

*Online-only material:* color figure

### 1. INTRODUCTION

Starburst galaxies are defined as galaxies that are currently undergoing a period of intense star formation, mainly within (but not exclusive to) the nuclear region, at a rate that cannot be maintained over their lifetime (Weedman 1987; Lehnert & Heckman 1996). The radio emission from such galaxies is not dominated by an active supermassive black hole, but by thermal and non-thermal emission that traces the star-forming activity (e.g., McDonald et al. 2002). The thermal emission is the result of free-free (or thermal bremsstrahlung) radiation from gas ionized by hot, young stars, while the non-thermal emission is from synchrotron radiation due to the acceleration of electrons to relativistic speeds by the core-collapse of massive stars to form Type II or Type Ibc supernovae (Pedlar et al. 1999; Weiler et al. 2002; McDonald et al. 2002). Interaction of the supernova with the local circumstellar medium generates a hot, shocked region that produces a prompt emission typically observed as a radio supernova (RSN; Weiler et al. 2002; Chevalier et al. 2006). As the RSNe expand into the surrounding interstellar medium, they evolve into supernova remnants (SNRs), forming shells that emit non-thermal synchrotron radiation that can be visible over many years (Woltjer 1972; Ulvestad & Antonucci 1997; Ferreira & de Jager 2008).

Studies of SNRs within nearby starburst galaxies can provide important information on the astrophysical processes occurring within these galaxies. Obscuration by dust and gas limit observations at shorter wavelengths, while radio wavelengths are largely unaffected. In addition, high-resolution, wide-field radio interferometry offers an opportunity to detect and resolve individual SNRs (e.g., McDonald et al. 2002; Tingay 2004; Lenc & Tingay 2006, 2009; Fenech et al. 2010). Such observations over

multiple epochs allow monitoring of the evolution of existing SNRs and the detection of new RSNe and/or SNRs, enabling the supernova and star formation history of the galaxy to be reconstructed. Such studies have been successfully applied to nearby starburst galaxies such as: M82 (Pedlar et al. 1999; McDonald et al. 2002; Beswick et al. 2006; Fenech et al. 2010; Gendre et al. 2013); Arp 220 (Rovilos et al. 2005; Lonsdale et al. 2006; Parra et al. 2007; Batejat et al. 2012); Arp 299 (Ulvestad 2009; Romero-Cañizales et al. 2011; Bondi et al. 2012); NGC 4945 (Lenc & Tingay 2009); and NGC 253 (Ulvestad & Antonucci 1997; Tingay 2004; Lenc & Tingay 2006). These studies have provided a wealth of information concerning RSNe and the evolution of SNRs, the star formation and supernova rates of the host galaxies, and the interstellar medium of the starburst region. For example, almost three decades of observations have identified  $\sim 100$  compact sources in M82 (Fenech et al. 2010), where most have been resolved into parsec-scale shell-like structures (Muxlow et al. 1994; Beswick et al. 2006; Fenech et al. 2010). In addition, these multi-epoch observations have been instrumental in measuring the expansion speeds of the resolved SNRs ( $2000\text{--}11,000 \text{ km s}^{-1}$ ), and in giving a direct estimate of the supernova rate ( $0.09 \text{ yr}^{-1}$ ) in M82. The discovery of new sources such as SN2008iz (Brunthaler et al. 2009b) and the radio transient 43.78+59.3 (Muxlow et al. 2010) would not have been possible without regular radio monitoring of M82. In addition, by combining multi-wavelength, high-resolution radio observations of 46 compact sources in M82, McDonald et al. (2002) were able to identify low-frequency spectral turnovers, due to free-free absorption by the surrounding ionized medium.

As one of the nearest star-forming galaxies, NGC 253 has been extensively studied from gamma-rays to radio wavelengths. Recently, as part of the Advanced Camera for Surveys

Nearby Galaxy Survey Treasury, Dalcanton et al. (2009) estimated the distance to NGC 253 as  $3.47 \pm 0.24$  Mpc,  $3.46 \pm 0.07$  Mpc, and  $3.40 \pm 0.09$  Mpc. The weighted average of the Dalcanton et al. (2009) distance estimates,  $3.44 \pm 0.13$  Mpc, is used as the distance to NGC 253 in this paper.

The first high-resolution, wide-field radio interferometric observations of NGC 253 were made by Turner & Ho (1985, hereafter TH85) with the Very Large Array (VLA) at 15 GHz (2 cm). With a resolution of  $0''.21 \times 0''.10$ , TH85 discovered nine compact sources (designated TH1 to TH9) within the central nuclear region. Following the results of TH85, Ulvestad and Antonucci conducted almost a decade of multi-frequency radio (1.8, 5, 8.3, 15, and 23 GHz) observations of the nuclear star-forming region of NGC 253 with the VLA, that culminated in a series of papers (Antonucci & Ulvestad 1988; Ulvestad & Antonucci 1991, 1994, 1997); they identified 64 individual compact sources, including the original nine from TH85. Spectral index measurements were obtained for the 17 brightest sources between frequency pairs of 5/15 and 8.3/23 GHz. Almost half of the 17 sources were identified with thermal H II regions while the remaining sources were taken to be associated with SNRs. Over the course of their survey, no new RSNe or SNRs appeared and the radio flux densities of the detected SNRs were found to be stable (Ulvestad & Antonucci 1997, hereafter UA97). This led to an estimate for the upper limit on the supernova rate of  $0.3 \text{ yr}^{-1}$  by UA97.

In an attempt to resolve the low-frequency radio emission in the inner 300 pc, Tingay (2004) conducted the first wide-field very long baseline interferometry (VLBI) observations of NGC 253. The observations were carried out with the Australian Long Baseline Array (LBA) at 1.4 GHz and matched the angular resolution of the UA97 23 GHz VLA observations. While the observations detected only two sources (TH7 and TH9), Tingay (2004) showed that the radio emission at low frequencies is absorbed by ionized gas with a free-free optical depth range at 1 GHz of  $\tau_0 \simeq 2.5$  to  $>8$ . This result was consistent with observations between 0.33 and 1.5 GHz with the VLA (Carilli 1996) and radio-recombination line modeling of the nuclear region of NGC 253 (Mohan et al. 2002).

Motivated by these indicators of free-free absorption in NGC 253, Lenc & Tingay (2006, hereafter LT06) began a program to observe the nuclear region of this galaxy with the LBA. Their observations, conducted in 2004 at 2.3 GHz, were higher in sensitivity and resolution than Tingay (2004) and covered the region observed by UA97. They identified six compact sources, which were also seen in the higher frequency observations with the VLA (UA97). One of the sources, 5.48-43.3 was also resolved into a shell-like structure approximately 90 mas (1.7 pc) in diameter. Combining the LT06 data with the multi-wavelength radio data from UA97, the spectra of 20 compact sources in the nuclear region of NGC 253 were found to be consistent with the free-free absorption interpretation of Tingay (2004). The results indicated that while the free-free optical depth is highest toward the supposed nucleus, it varies significantly ( $\tau_0 \simeq 1$  to  $>20$ ) throughout the nuclear region, implying variations in the gas density. Of the 20 sources, eight were found to have flat spectral indices, indicative of thermal H II regions, while the remaining sources were taken to be associated with SNRs due to their steep spectral indices at high frequencies. With no new sources detected in NGC 253 over almost two decades, LT06 developed a Monte Carlo method based on the work of Ulvestad & Antonucci (1991), to estimate the upper limit on the supernova rate. Their model took into consideration

improved distance measurements, a median free-free opacity, and the sensitivity limits of six observations over a 17 yr period. A value of  $2.4 \text{ yr}^{-1}$  was derived for the upper limit on the supernova rate. This high value suggests that there may be a large number of undetected RSNe, with observations over that period only detecting the rare, bright events. Detecting weaker or short-lived SNRs would provide tighter constraints on the supernova rate. However, this can only be done through frequent, high-sensitivity, high-resolution observations of NGC 253.

In this paper, we present the results of multi-epoch, wide-field VLBI observations conducted at 2.3 GHz with the LBA, of the nuclear region of NGC 253. Section 2 describes the observations, data analysis methods, and the sources detected, including cross identifications with previous observations and investigations of possible flux density variations. Free-free absorption modeling of the spectra is described in Section 3.1. The morphology of the resolved SNR, 5.48-43.3, is examined in detail in Section 3.2. An improvement to the Monte Carlo method of LT06 is presented with new estimates of the upper limits on supernova and star formation rates (SFRs) within the inner 300 pc region of NGC 253 in Sections 3.3 and 3.4. The results are summarized in Section 4.

## 2. OBSERVATIONS, DATA REDUCTION, AND RESULTS

### 2.1. Observations

NGC 253 was observed at 2.3 GHz with the Australian LBA, at three epochs as described in Table 1. The observations were carried out with: the 64 m Parkes (Pa) antenna of the Australia Telescope National Facility (ATNF); the ATNF Australia Telescope Compact Array (ATCA),<sup>4</sup> used as a phased array; the ATNF Mopra (Mp) 22 m antenna; and the University of Tasmania's 26 m antenna near Hobart (Ho); and the University of Tasmania's 30 m antenna near Ceduna (Cd). In addition, the 70 m NASA Deep Space Network antenna at Tidbinbilla (Tid) was used for the 2008 epoch. The data for each observation were recorded from  $4 \times 16$  MHz bands (digitally filtered two-bit samples) in the frequency ranges given in Table 1. All bands had dual circular polarization at Parkes, ATCA, and Mopra, with right circular polarization only at the remaining antennas. Table 1 lists the parameters associated with the LBA observations. During each observation, 3 minute scans of NGC 253 (centered on:  $\alpha = 00^{\text{h}}47^{\text{m}}33\rlap{.}^{\text{s}}178$ ;  $\delta = -25^{\circ}17'17\rlap{.}^{\text{s}}060$  [J2000.0]) were scheduled, alternating with 3 minute scans of a nearby phase reference calibration source, PKS J0038-2459 ( $\alpha = 00^{\text{h}}38^{\text{m}}14\rlap{.}^{\text{s}}735$ ;  $\delta = -24^{\circ}59'02\rlap{.}^{\text{s}}235$  [J2000.0]), located  $2^\circ 13'$  from the target. The recorded data for all epochs were correlated using the DiFX software correlator (Deller et al. 2007, 2011), with an integration time of 2 s and 64 frequency channels across each 16 MHz band (channel widths of 0.25 MHz). The  $uv$  coverage for the 2007 and 2008 epochs is shown in Figure 1.

### 2.2. Calibration and Data Reduction

The initial data reduction and calibration were performed using the data reduction package AIPS.<sup>5</sup> Prior to calibration, flagging of data during times at which each of the antennas were known to be slewing and time ranges that contained known

<sup>4</sup>  $5 \times 22$  m antennas were used for the 2006 and 2008 epochs, while  $4 \times 22$  m antennas were used for the 2007 epoch.

<sup>5</sup> The Astronomical Image Processing System was developed and is maintained by the National Radio Astronomy Observatory, which is operated by Associated Universities, Inc., under cooperative agreement with the National Science Foundation.

**Table 1**  
2.3 GHz LBA Multi-epoch Observations

Epoch	2006	2007	2008
Observing date	May 12/13	June 22/23	June 5/6
Array	PA ATCA MP CD HO	PA ATCA MP CD HO	PA ATCA MP CD HO TID
Observing time (hr)	12	12	10
Frequency range (MHz)	2269-2333	2268-2332	2226-2290
Bandwidth (MHz)	64	64	64
No. of IFs × no. of frequency channels	4×16	4×16	4×16
Polarization (PA ATCA MP)	RR LL	RR LL	RR LL
Polarization (CD HO TID)	RR	RR	RR
Naturally weighted wide-field array rms (mJy beam <sup>-1</sup> )	0.39	0.44	0.18
Wide-field array CLEAN beam (mas)	147×51 @ -71°	134×48 @ -72°	86×33 @ -88°
Full array CLEAN beam (mas)	15×13 @ 0°	15×15 @ -29°	16×13 @ 37°

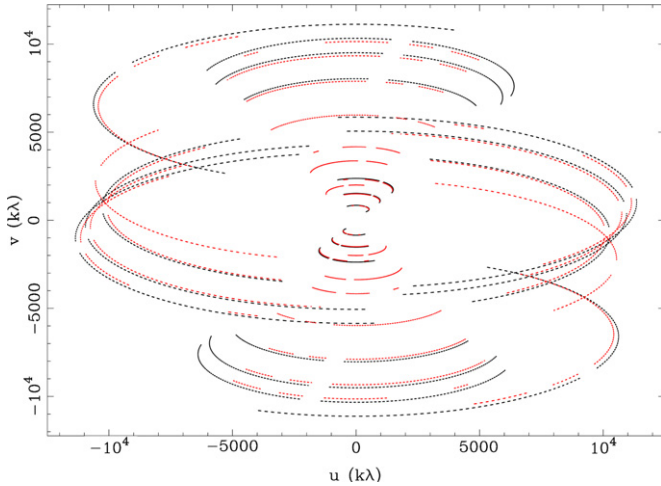


**Figure 1.** *uv* coverage of the 2007 (black) and 2008 (red) LBA epochs at 2.3 GHz (band center frequency for each baseline only). The *uv* coverage for the 2006 epoch (not plotted) was similar to the 2007 *uv* coverage.  
(A color version of this figure is available in the online journal.)

bad data, were carried out via application of flag files and information provided by the observing logs. Data from the first 30 s of each scan from baselines involving ATCA or Parkes were flagged, in order to eliminate known corruption of the data at the start of each scan at these two telescopes.

During correlation, nominal (constant) system temperatures (in Jansky) for each antenna were applied to the correlation coefficients. The nominal calibration was refined by application of antenna system temperatures (in Kelvin) measured during the observation, along with the gain (in Janskys per Kelvin) for each antenna. Further refinements to the amplitude calibration were derived from simultaneously recorded ATCA observations of PKS J0038-2459, which is a bright, compact radio source, unresolved at this frequency on the LBA baselines. Since the LBA is not resolving out any extended structure, the ATCA and LBA baselines will measure the same flux density. Thus, the flux density measured at the ATCA can be used to check and refine the amplitude calibration for the LBA data. Suitable simultaneous recorded ATCA data were obtained for all but the 2008 observation.

The NRAO's Very Long Baseline Array calibrator survey routinely observes PKS J0038-2459 at 2.3 GHz, but did not in 2008. Figure 2 plots the 2.3 GHz light curve of PKS J0038-2459 for eight epochs from 1997 to 2010. The error bars are  $\pm 10\%$  of the measured flux densities. A weighted non-linear least-squares fit was used to interpolate to the flux density of PKS

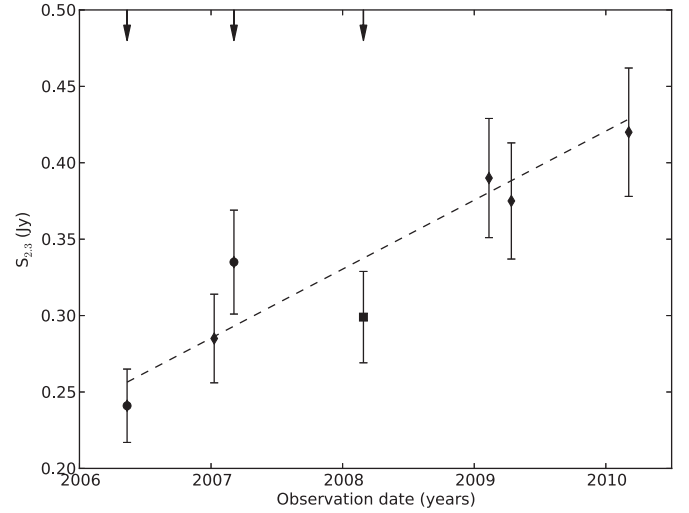


**Figure 2.** Light curve of the PKS J0038-2459 from 2006 to 2010 at 2.3 GHz. The data are from the Bordeaux VLBI Image Database and the USNO Radio Reference Frame Image Database (points) and the LBA fluxes derived from our 2006 and 2007 observations (circles). A non-linear least-squares fit to the data was used to interpolate the flux density of the calibrator during the 2008 epoch. The resulting fit produced a standard deviation,  $\sigma = 19$  mJy. The square point plots the final imaged flux density following amplitude refinement for the 2008 epoch (square). The arrows indicate the dates of the LBA observations.

J0038-2459 at the time of the 2008 LBA observation. The fit gave a flux density of 337 mJy, with a  $1\sigma$  error of 19 mJy at the time of the 2008 observation. This flux density was used to refine the amplitude calibration for the 2008 LBA data, by defining a model with this flux density in DIFMAP (Shepherd 1997). The DIFMAP task GSCALE was used to determine corrections to the uncalibrated amplitudes of PKS J0038-2459 from the model.

Following amplitude calibration refinement, global fringe-fitting solutions were determined for PKS J0038-2459 (AIPS task FRING) with a three minute solution interval, finding independent solutions for each of the 16 MHz bands. The delay and phase solutions were examined and, following editing of bad solutions, applied to PKS J0038-2459. The PKS J0038-2459 data were exported to DIFMAP, where the data were vector-averaged over 30 s, flagged of bad data, and imaged using standard imaging techniques (deconvolution and self-calibration of both phase and amplitude). The resulting images of PKS J0038-2459 for the 2006–2008 epochs show a highly compact source, with no significant structure on these baselines at this frequency to a dynamic range<sup>6</sup> of 400. The final calibration

<sup>6</sup> Defined as the ratio of the peak of the image to the peak of brightest artifact.

solutions (phase and amplitude) of PKS J0038–2459 were exported via the DIFMAP task CORDUMP<sup>7</sup> (Lenc & Tingay 2009) to an AIPS-compatible solutions table. The solutions table was then transferred to AIPS and applied to all sources in the data set. The PKS J0038–2459 data were also used to derive a bandpass calibration via the AIPS task BPASS which was applied to the NGC 253 data. The edge channels of each band were flagged from the data set (2 channels from both the lower and upper edge of each 16 channel band). The final calibration solutions were applied to both PKS J0038–2459 and NGC 253 and the visibility data exported as FITS files.

The loss of amplitude due to bandwidth smearing at the field's edge (radius of  $\sim 10''$  from the phase center) is  $\sim 3\%$  on the longest baseline (Hobart–Ceduna). Thus, to allow imaging of the inner 300 pc at a resolution of  $\sim 15$  milli-arcseconds (mas), the NGC 253 data set was not averaged in time or frequency. To facilitate imaging in DIFMAP, the frequency channels were converted into intermediate frequencies (IFs). This conversion allowed DIFMAP to treat the frequency channels independently in the  $uv$  plane rather than averaging them together, thus avoiding any further bandwidth smearing effects during the imaging process.

NGC 253 imaging was initially performed with a reduced resolution by excluding data from the Hobart and Ceduna antennas (the longest baselines). The imaging parameters were chosen to closely match the imaging parameters of LT06, with cell size of 11 mas and application of natural weighting to minimize noise at the expense of resolution. Figure 3 displays the resulting contour images of NGC 253 for the three epochs. The  $1\sigma$  noise measurements for the three images are listed in Table 1. The  $1\sigma$  noise levels at the 2006 and 2007 epochs are 2–3 times higher than at the 2008 epoch, which can be attributed to the absence of the 70 m Tidbinbilla antenna in 2006/2007. However, the  $1\sigma$  noise of the 2008 image is 28% lower than that of the LT06 (2004 epoch) image due to increased bandwidth.

Figure 4 shows the images of the SNR 5.48-43.3 for the three epochs. The images were made with the full array (i.e., including data from both Hobart and Ceduna), with natural weighting and a cell size of 4 mas.

### 2.3. Identification of Sources and Flux Density Measurements

A number of detected sources are clearly visible in Figure 3. We used the source extraction software BLOBCAT (Hales et al. 2012) to identify and measure the flux densities of compact sources in the three images. Seven sources were detected above  $5\sigma$  by BLOBCAT in the 2008 epoch, while only the three brightest sources (5.48-43.3, 5.62-41.3, and 5.79-39.0) were found via BLOBCAT for the less sensitive 2006 and 2007 epochs (see Table 2).

Included in Table 2 are the flux densities for the compact sources detected in the 2004 epoch by LT06. Only three of these sources were detected in all four 2.3 GHz LBA epochs (i.e., 2004, 2006, 2007, and 2008), while three were detected in only the 2004 and 2008 epochs, with one possible additional source detected solely in the 2008 image. The flux density of the sources detected by LT06 were also estimated via BLOBCAT and found to agree with LT06's values within measurement errors. For comparison, the published source flux densities of LT06 are included in Table 2. While stacking of the 2004 and 2008 images improved image noise by a factor of  $\sqrt{2}$ , the resulting image did not reveal any additional sources.

<sup>7</sup> <http://www.atnf.csiro.au/people/Emil.Lenc/tools/Tools/Cordump.html>

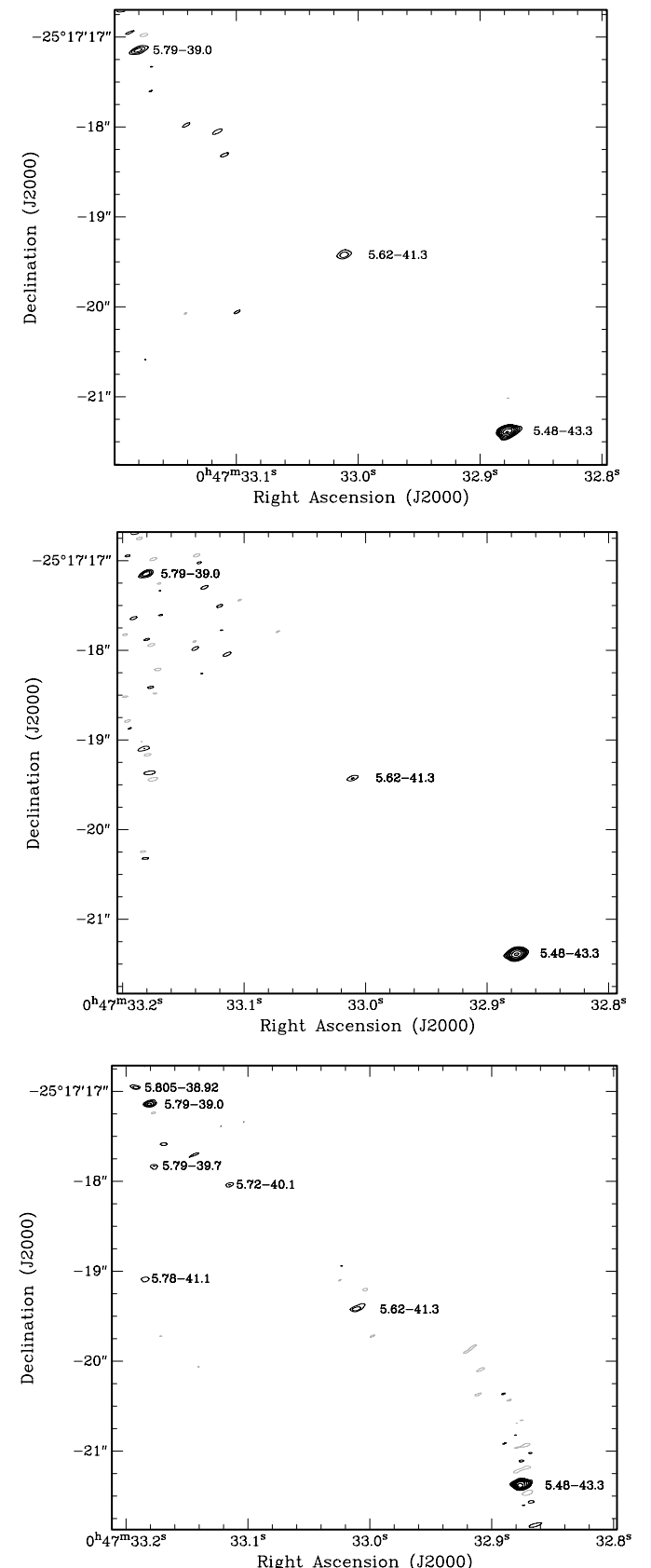


**Figure 3.** Wide-field VLBI images of NGC 253 with the LBA at 2.3 GHz. Top: 2006 epoch. The rms noise level is  $0.39 \text{ mJy beam}^{-1}$ . The peak is  $10.4 \text{ mJy beam}^{-1}$ . Middle: 2007 epoch. The rms noise level is  $0.44 \text{ mJy beam}^{-1}$ . The peak is  $11.8 \text{ mJy beam}^{-1}$ . Bottom: 2008 epoch. The rms noise level is  $0.18 \text{ mJy beam}^{-1}$ . The peak is  $7.9 \text{ mJy beam}^{-1}$ . The contours in the three plots are  $[-3\sqrt{2}\sigma, 3(\sqrt{2})^n\sigma]$ , where  $\sigma$  is the rms noise of each image and  $n = 1, 2, 3, \dots, 7$ .

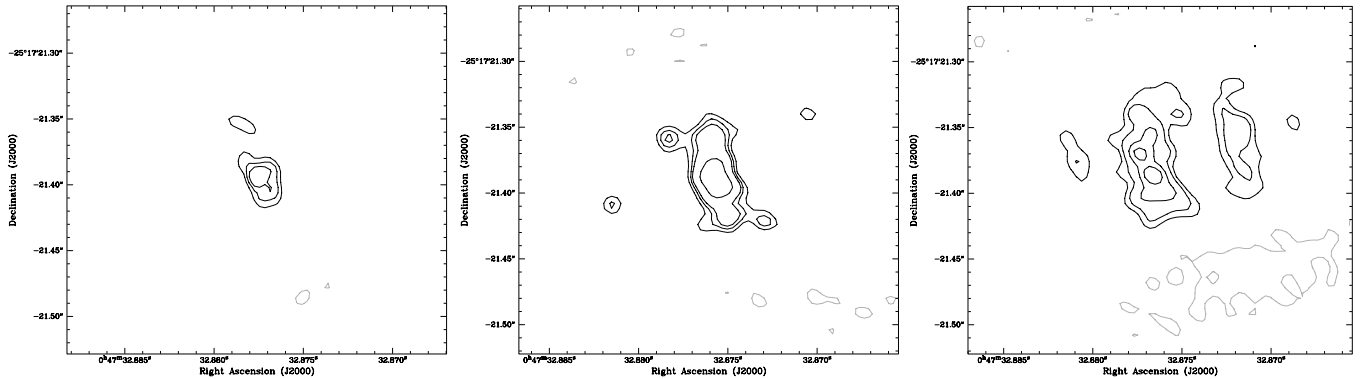


**Figure 4.** 2.3 GHz Australian LBA images of 5.48-43.3. Left: 2006 epoch. The rms noise of the image is  $0.22 \text{ mJy beam}^{-1}$  and the peak flux density is  $1.6 \text{ mJy beam}^{-1}$ . The beam size is  $15 \times 14 \text{ mas}$  at a position angle (PA) of  $0^\circ 1$ . Center: 2007 epoch. The rms noise of the image is  $0.26 \text{ mJy beam}^{-1}$  and the peak flux density is  $3.8 \text{ mJy beam}^{-1}$ . The beam size is  $15 \times 14 \text{ mas}$  at a PA of  $-85^\circ$ . Right: 2008 epoch. The rms noise of the image is  $0.13 \text{ mJy beam}^{-1}$  and the peak flux density is  $2.61 \text{ mJy beam}^{-1}$ . The beam size is  $16 \times 13 \text{ mas}$  at a PA of  $37^\circ$ . The contours of the three epochs are  $[-3\sigma_{\text{rms}}, n\sigma_{\text{rms}}]$ , where  $n = 3, 4, 5, 10, 15$  and  $\sigma_{\text{rms}}$  is the respective image rms.

**Table 2**  
Compact Sources Detected with the LBA at 2.3 GHz

Position <sup>a</sup>		Identification <sup>b</sup>			Peak Flux Density (mJy beam <sup>-1</sup> )				Integrated Flux Density (mJy)			
$\alpha$ (J2000.0)	$\delta$ (J2000.0)	UA97	TH85	LT06 <sup>c</sup>	$S_P^{2004d}$	$S_P^{2006}$	$S_P^{2007}$	$S_P^{2008}$	$S_I^{2004e}$	$S_I^{2006}$	$S_I^{2007}$	$S_I^{2008}$
(00h47 <sup>m</sup> )	(-25°17')											
32.876	21.383	5.48-43.3	TH9	Y	$8.6 \pm 0.9$	$13.5 \pm 1.6$	$16.0 \pm 1.9$	$7.8 \pm 0.2$	$32.0 \pm 3.2$	$22.8 \pm 2.4$	$30.2 \pm 3.4$	$25.1 \pm 9.9$
33.012	19.425	5.62-41.3	TH7	Y	$1.7 \pm 0.2$	$2.7 \pm 0.6$	$2.4 \pm 0.5$	$1.3 \pm 0.3$	$8.8 \pm 0.9$	$6.3 \pm 0.8$	$5.7 \pm 0.8$	$6.8 \pm 2.7$
33.115	18.039	5.72-40.1	TH6	Y	$1.5 \pm 0.2$	<2.0	<2.2	$1.0 \pm 0.2$	$3.8 \pm 0.4$	<2.0	<2.2	$3.0 \pm 1.2$
33.185	19.084	5.78-41.1	...	N	<1.2	<2.0	<2.2	$0.9 \pm 0.2$	<1.2	<2.0	<2.2	$4.6 \pm 1.8$
33.177	17.830	5.79-39.7	TH3	Y	$1.8 \pm 0.2$	<2.0	<2.2	$1.0 \pm 0.2$	$6.2 \pm 0.6$	<2.0	<2.2	$3.2 \pm 1.3$
33.181	17.148	5.79-39.0	TH2	Y	$2.4 \pm 0.2$	$4.1 \pm 0.6$	$4.9 \pm 0.7$	$2.6 \pm 0.4$	$5.7 \pm 0.6$	$7.8 \pm 1.0$	$7.3 \pm 0.9$	$5.9 \pm 2.3$
33.193	16.949	5.805-38.92	...	Y	$2.1 \pm 0.2$	<2.0	<2.2	$1.5 \pm 0.3$	$6.8 \pm 0.7$	<2.0	<2.2	$2.4 \pm 1.0$

#### Notes.

<sup>a</sup> The measured 2.3 GHz source positions for the 2008 epoch. Units of right ascension are seconds and units of declination are arcseconds.

<sup>b</sup> Source identifications with 1.3 and 2 cm sources from UA97, and 2 cm sources from TH85.

<sup>c</sup> Detected (Y) or not detected (N) by LT06.

<sup>d</sup> Acquired from LT06.

<sup>e</sup> Acquired from LT06.

Errors in the flux-density estimates have two different origins. First, there is the overall uncertainty in the absolute flux density scale for the LBA, estimated as  $\pm 10\%$  (Reynolds 1994). Second, there are the errors in determining the flux density by BLOBCAT, which ranges from 5% to 10%. Both terms are added in quadrature for the 2006 and 2007 observations. For the 2008 observation, we determine a third contribution to the error, which is described in Section 2.3.1.

Table 2 lists cross identifications with sources detected at 15 GHz and 23 GHz by UA97 and at 2.3 GHz with the LBA by LT06. The mean position difference between our 2008 and LT06's 2004 J2000.0 source positions was found to be 8 mas, with a standard deviation of 5 mas, which is  $\sim 10\%$  of the beam-width. The mean position difference between our 2008 J2000.0 source position and the B1950.0 source positions of the 23 GHz sources from UA97 is 87 mas, with a standard deviation of 51 mas.

#### 2.3.1. Variations in the Flux Density

Lower integrated flux densities are recorded for all sources except for 5.79-39.0 in the 2008 epoch compared to the 2004 epoch (see Table 2 and Figure 5). Since it was necessary to interpolate the flux density of a variable calibrator to obtain

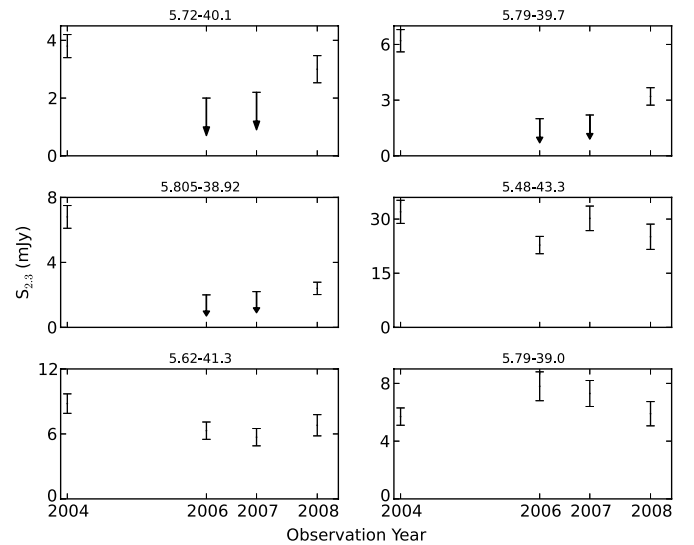


**Figure 5.** Light curves of the compact sources detected in all 2.3 GHz observations (2004, 2006, 2007, and 2008). The integrated flux densities (from Table 2) are plotted on the y-axis, while the observation date is listed on the x-axis.  $5\sigma$  upper limits are represented by arrows for epochs without detections. The error bars are the absolute flux density scaling and measurement errors (see Section 2.3) added in quadrature.

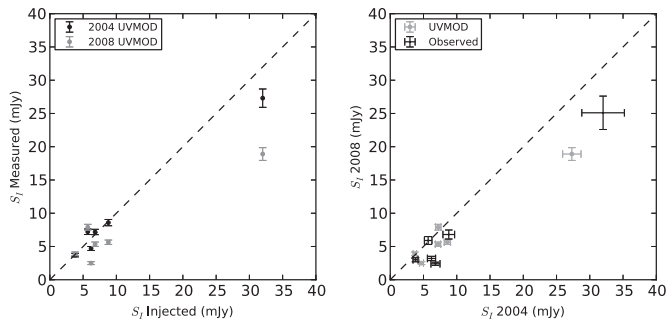


**Figure 6.** Left: the integrated flux densities of the fake sources (x-axis) injected into the modeled data sets via UVMOD are plotted against the recovered integrated flux densities for the 2004 (black points) and 2008 (gray points) modeled data sets. Right: the recovered integrated flux densities of the fake sources for the 2004 and 2008 modeled data sets (gray points) are compared, while the observed integrated flux densities from Table 2 for the same epochs (black points). The dashed lines represent where  $y = x$ .

a value for the 2008 epoch (see Section 2.2) it would not be surprising if there were an error on the flux density scale. Given the covariance of the flux densities between 2006 and 2008 (and possibly for the other epochs too) this would appear to be the case. Adjusting empirically for the difference in flux density between 2006 and 2008 by taking the mean of each, we find that we must increase the absolute flux density calibration of the 2008 epoch by 20%. After this adjustment, no source appears significantly variable with the exception of 5.805–38.92, whose decrease in flux density would still be a  $9\sigma$  error (assuming of course that the distribution of the errors is Gaussian).

To investigate whether the flux density decrease is genuine we used the AIPS task UVMOD to simulate data sets with the same  $uv$  coverage and noise level as the 2004 and 2008 LBA data sets. In UVMOD the parameter FACTOR was set to zero to allow the injection of the fake sources at the same positions as the real ones. The fake sources were injected with the properties (i.e., size, position angle, integrated flux density, and position) of the sources detected by LT06. The resulting data sets were exported and imaged in DIFMAP following the procedure described in Section 2.2. The integrated flux densities of the injected sources were measured with BLOBCAT and plotted in Figure 6 (left plot) against the model flux densities. If the flux density decrease in the observed data set were due to only source variability, the measured (or recovered) flux densities would be equal to the injected flux densities, represented by the dashed lines. The deviation of the UVMOD flux densities from the dashed lines follows a similar trend to the observed flux densities (right plot of Figure 6). Thus it is possible the flux density decrease results mainly from systematic effects such as deconvolution errors (e.g., CLEAN bias; Becker et al. 1995) and high side-lobes.

The effect of CLEAN bias is known to produce a systematic underestimation of flux densities (Becker et al. 1995) by redistributing flux density from sources to noise peaks in the image during deconvolution. The magnitude of the flux density redistributed is generally independent of flux density, and thus the fractional error is largest for weak sources. This effect may have a stronger effect in the 2008 image (as compared to the 2004 image) due to the presence of high side-lobes. The high side-lobes may have resulted from the combination of poor  $uv$  coverage and an increased sensitivity due to a higher bandwidth.

The rms<sup>8</sup> difference between the 2008 recovered flux densities and the model flux densities is 37%, which is added in

quadrature with the absolute flux density scaling and measurement errors for the 2008 epoch (see Section 2.3) and listed in Table 2. The resulting flux density decrease of 5.805–38.92 is then reduced to a significance of  $4.5\sigma$ . While this variability may be due to unaccounted for calibration errors, we cannot rule out contributions from intrinsic variability.

### 3. DISCUSSION

#### 3.1. Radio Spectra and Free–Free Absorption Modeling of Compact Sources in NGC 253

A downturn in the spectra of the compact sources in NGC 253 at low frequencies was observed previously by Tingay (2004) and LT06. Different mechanisms were explored by LT06 to explain the observed effect, including a simple power law, a power-law spectrum with free–free absorption by a screen of ionized gas, and a self-absorbed bremsstrahlung spectrum. LT06 demonstrated that the spectra of the sources were consistent with a free–free absorbed power-law spectrum, given by the following equation:

$$S(\nu) = S_0 \nu^\alpha e^{-\tau(\nu)}, \quad (1)$$

where

$$\tau(\nu) = \tau_0 \nu^{-2.1} \quad (2)$$

and  $\alpha$  is the optically thin intrinsic spectral index,  $\tau_0$  is the free–free optical depth at 1 GHz, and  $S_0$  is the intrinsic flux density of the source at 1 GHz. Similar spectra have been obtained for compact sources in other nearby starburst galaxies, such as M82 (McDonald et al. 2002), Arp 220 (Parra et al. 2007), and NGC 4945 (Lenc & Tingay 2009). We therefore adopt this model and the method described by LT06.

To model the free–free absorption toward the compact sources within NGC 253 we compile multi-wavelength radio flux density measurements for these sources from the literature (listed in Table 3), including: 1.4 GHz LBA data (Tingay 2004); 2.3 GHz LBA data (LT06 and this paper); and 23 GHz, 15 GHz, 8.3 GHz, and 5 GHz VLA data (UA97).

Brunthaler et al. (2009a) detected 10 UA97 sources at 23 GHz with the VLA (A configuration) in 2004. They reported higher flux densities for all sources compared to UA97, at the same frequency. Only the source 5.79–39.0 (the assumed core TH2) was similar in both epochs within a 10% error. The authors attributed the higher flux densities in their data to a larger beam ( $\sim 40\%$ ). To keep the spectral modeling consistent with LT06 and maintain a comparable beam size with the LBA 2.3 GHz images, the flux densities from Brunthaler et al. (2009a) were not used.

Figure 7 presents multi-epoch monitoring of the free–free spectra of 20 compact sources in NGC 253. The free–free spectra obtained by LT06 are plotted as dashed lines, while the solid lines are the spectra derived using the 2008 2.3 GHz LBA data. For sources not detected in the 2008 observation, an upper limit of  $0.9 \text{ mJy beam}^{-1}$  ( $5\sigma$ ) was adopted. Table 4 lists the fitted free parameters  $\alpha$ ,  $\tau_0$ , and  $S_0$  for each compact source. Included for reference are the values of the parameters for the 2004 data. Differences in the free–free spectra and derived parameters between 2004 and 2008, while potentially large, are still within our errors, suggesting no evidence for changes in the free–free absorbing medium between epochs. These results further confirm the free–free absorption interpretation of Tingay (2004) and LT06.

<sup>8</sup> We define the root mean square (rms) difference between the modeled and the recovered flux densities, as  $\sqrt{1/n \sum (S_{\text{model}} - S_{\text{recovered}})^2 / S_{\text{model}}}$ .

**Table 3**  
Summary of Flux Density Measurements for Radio Sources in NGC 253

VLA ID	LBA <sup>a</sup> (mJy)					VLA <sup>b</sup> (mJy)				
	$S_{1.4}$	$S_{2.3}^{2004}$	$S_{2.3}^{2006}$	$S_{2.3}^{2007}$	$S_{2.3}^{2008}$	$S_5$	$S_{8.3}$	$S_{15}$	$S_{23}$	$S_{23}^{\text{BCT}}$
4.81-43.6	<1.8	<1.2	<2.0	<2.2	<0.9	$1.4 \pm 0.2$	...	$0.4 \pm 0.3$	...	$1.4 \pm 0.3$
5.48-43.3	$16 \pm 0.2$	$32.0 \pm 3.2$	$22.8 \pm 2.4$	$30.2 \pm 3.4$	$25.1 \pm 9.9$	$27.1 \pm 2.7$	$20.5 \pm 1.0$	$12.5 \pm 1.3$	$9.8 \pm 1.0$	$13.1 \pm 0.9$
5.49-42.2	<1.8	<1.2	<2.0	<2.2	<0.9	...	$1.1 \pm 0.2$	...	0.8	...
5.54-42.2	<1.8	<1.2	<2.0	<2.2	<0.9	$2.8 \pm 0.4$	$2.7 \pm 0.24$	$3.4 \pm 0.4$	$4.5 \pm 0.5$	$9.2 \pm 1.7$
5.59-41.6	<1.8	<1.2	<2.0	<2.2	<0.9	...	$3.0 \pm 0.3$	...	5.7	...
5.62-41.3	$6.0 \pm 0.6$	$8.8 \pm 0.9$	$6.3 \pm 0.8$	$5.7 \pm 0.8$	$6.8 \pm 2.7$	$9.8 \pm 1.0$	$7.3 \pm 0.4$	$7.5 \pm 0.8$	$5.8 \pm 0.6$	$10.7 \pm 1.4$
5.65-40.7	<1.8	<1.2	<2.0	<2.2	<0.9	...	$1.5 \pm 0.2$	...	$1.2 \pm 0.3$	...
5.72-40.1	<1.8	$3.8 \pm 0.4$	<2.0	<2.2	$3.0 \pm 1.2$	$7.7 \pm 0.8$	$6.5 \pm 0.4$	$7.8 \pm 0.8$	$7.9 \pm 0.8$	$21.9 \pm 2.3$
5.73-39.5	<1.8	<1.2	<2.0	<2.2	<0.9	...	$2.4 \pm 0.2$	...	$2.8 \pm 0.4$	...
5.75-41.8	<1.8	<1.2	<2.0	<2.2	<0.9	$7.0 \pm 0.7$	$4.8 \pm 0.3$	$3.1 \pm 0.4$	$2.6 \pm 0.4$	...
5.78-39.4	<1.8	<1.2	<2.0	<2.2	<0.9	...	$16.9 \pm 0.9$	...	$9.7 \pm 1.0$	$29.9 \pm 1.2$
5.79-39.0	<1.8	$5.7 \pm 0.6$	$7.8 \pm 1.0$	$7.3 \pm 0.9$	$5.9 \pm 2.3$	$38.6 \pm 3.9$	$48.0 \pm 2.4$	$40.3 \pm 4.0$	$35.8 \pm 3.6$	$38.4 \pm 0.9$
5.79-39.7	<1.8	$6.2 \pm 0.6$	<2.0	<2.2	$3.2 \pm 1.3$	...	...	$\sim 4.1 \pm 0.5$	$\sim 1.6 \pm 0.3$	...
5.78-41.1	<1.8	<1.2	<2.0	<2.2	$4.6 \pm 1.8$	$4.7 \pm 0.5$	$3.2 \pm 0.3$	$1.9 \pm 0.3$	$1.0 \pm 0.3$	...
5.805-38.92	<1.8	$6.8 \pm 0.7$	<2.0	<2.2	$2.4 \pm 1.0$	...	...	$\sim 3.0 \pm 0.4$	$\sim 1.9 \pm 0.3$	$8.9 \pm 1.1$
5.87-40.1	<1.8	<1.2	<2.0	<2.2	<0.9	$3.8 \pm 0.4$	$2.1 \pm 0.2$	$1.4 \pm 0.3$	$0.7 \pm 0.3$	...
5.90-37.4	<1.8	<1.2	<2.0	<2.2	<0.9	$4.0 \pm 0.5$	$4.0 \pm 0.3$	$5.9 \pm 0.7$	$6.7 \pm 0.7$	$9.1 \pm 1.2$
5.95-37.7	<1.8	<1.2	<2.0	<2.2	<0.9	$1.2 \pm 0.2$	...	$0.6 \pm 0.3$	...	...
6.00-37.0	<1.8	<1.2	<2.0	<2.2	<0.9	$5.9 \pm 0.6$	$3.5 \pm 0.2$	$2.4 \pm 0.4$	$1.7 \pm 0.3$	...
6.40-37.1	<1.8	<1.2	<2.0	<2.2	<0.9	$2.9 \pm 0.4$	...	$1.3 \pm 0.3$	...	$0.8 \pm 0.2$

**Notes.**

<sup>a</sup>  $S_{1.4}$  is the measured flux density from the LBA (Tingay 2004),  $S_{2.3}$  are the measured flux density at 2.3 GHz from 2004 (LT06) and this work (2006–2008), where the superscript indicates the observation year. Upper limits on the flux ( $5\sigma$ ) are provided for sources that have not been detected.

<sup>b</sup>  $S_5$ ,  $S_{8.3}$ ,  $S_{15}$ , and  $S_{23}$  are the measured 5, 8.3, 15, and 23 GHz flux densities from the VLA by UA97 and  $S_{23}^{\text{BCT}}$  are the 23 GHz VLA flux densities of Brunthaler et al. (2009a).

**Table 4**  
Parameters of the Free–Free Absorption Models for All Compact Sources

Source	$S_0^{2004}$	$\alpha^{2004}$	$\tau^{2004}$	Type <sup>a</sup>	$S_0^{2008}$	$\alpha^{2008}$	$\tau^{2008}$	Type
4.81-43.6	$19.92 \pm 12.81$	$-1.46 \pm 0.62$	$9.16 \pm 5.16$	S	$24.1 \pm 16.4$	$-1.53 \pm 0.73$	$11.59 \pm 6.84$	S
5.48-43.3	$105.6 \pm 0.3$	$-0.77 \pm 0.01$	$3.30 \pm 0.02$	S	$76.4 \pm 0.13$	$-0.63 \pm 0.01$	$2.89 \pm 0.01$	S
5.49-42.2	$2.31 \pm 0.53$	$-0.33 \pm 0.15$	$2.19 \pm 1.65$	T	$2.47 \pm 0.84$	$-0.35 \pm 0.24$	$4.12 \pm 3.11$	T
5.54-42.2	$1.54 \pm 0.18$	$0.33 \pm 0.06$	$2.54 \pm 1.66$	T	$1.68 \pm 0.30$	$0.3 \pm 0.09$	$4.21 \pm 2.60$	T
5.59-41.6	$0.72 \pm 0.04$	$0.67 \pm 0.03$	$0.29 \pm 1.12$	T	$0.77 \pm 0.11$	$0.65 \pm 0.07$	$2.23 \pm 2.30$	T
5.62-41.3	$16.11 \pm 0.04$	$-0.31 \pm 0.01$	$1.82 \pm 0.02$	T	$12.25 \pm 0.07$	$-0.21 \pm 0.01$	$1.49 \pm 0.02$	T
5.65-40.7	$2.71 \pm 0.73$	$-0.25 \pm 0.17$	$3.46 \pm 2.28$	T	$2.89 \pm 1.02$	$-0.27 \pm 0.24$	$5.40 \pm 3.66$	T
5.72-40.1	$8.25 \pm 0.37$	$-0.02 \pm 0.02$	$4.12 \pm 0.53$	T	$9.03 \pm 0.94$	$-0.05 \pm 0.04$	$5.70 \pm 1.23$	T
5.73-39.5	$2.07 \pm 0.47$	$0.09 \pm 0.12$	$3.59 \pm 2.33$	T	$2.21 \pm 0.65$	$0.07 \pm 0.17$	$5.52 \pm 3.58$	T
5.75-41.8	$76.97 \pm 5.12$	$-1.16 \pm 0.04$	$17.46 \pm 0.64$	S	$86.16 \pm 5.80$	$-1.20 \pm 0.04$	$18.98 \pm 0.66$	S
5.78-39.4	$121.18 \pm 2.49$	$-0.81 \pm 0.01$	$22.67 \pm 0.51$	S	$129.41 \pm 3.35$	$-0.83 \pm 0.01$	$24.61 \pm 0.67$	S
5.79-39.0	$150.79 \pm 0.59$	$-0.46 \pm 0.01$	$17.58 \pm 0.08$	S	$149.60 \pm 2.32$	$-0.46 \pm 0.01$	$17.45 \pm 0.26$	S
5.79-39.7	$4899.0 \pm 2737.6$	$-2.58 \pm 0.93$	$25.15 \pm 10.52$	S	$5244.7 \pm 2959.9$	$-2.6 \pm 1.14$	$30.09 \pm 13.9$	S
5.78-41.1	$75.97 \pm 5.53$	$-1.38 \pm 0.04$	$17.09 \pm 0.60$	S	$33.03 \pm 4.71$	$-1.07 \pm 0.08$	$6.20 \pm 0.88$	S
5.805-38.92	$87.74 \pm 25.72$	$-1.23 \pm 0.15$	$8.26 \pm 1.68$	S	$97.7 \pm 49.61$	$-1.27 \pm 0.55$	$15.24 \pm 7.14$	S
5.87-40.1	$70.27 \pm 36.82$	$-1.50 \pm 0.51$	$16.00 \pm 6.63$	S	$84.0 \pm 16.12$	$-1.57 \pm 0.11$	$18.17 \pm 1.33$	S
5.90-37.4	$2.30 \pm 0.35$	$0.35 \pm 0.07$	$4.72 \pm 2.30$	T	$2.48 \pm 0.48$	$0.32 \pm 0.09$	$6.20 \pm 3.05$	T
5.95-37.7	$5.08 \pm 1.94$	$-0.80 \pm 0.30$	$4.45 \pm 2.67$	S	$6.15 \pm 2.89$	$-0.87 \pm 0.42$	$6.89 \pm 4.37$	S
6.00-37.0	$82.41 \pm 8.22$	$-1.32 \pm 0.05$	$17.28 \pm 0.80$	S	$94.1 \pm 9.4$	$-1.37 \pm 0.05$	$18.98 \pm 0.82$	S
6.40-37.1	$25.72 \pm 12.40$	$-1.10 \pm 0.47$	$12.35 \pm 5.91$	S	$31.17 \pm 15.94$	$-1.17 \pm 0.55$	$14.78 \pm 7.40$	S

**Notes.** The superscript indicates the LBA 2.3 GHz epoch.

<sup>a</sup> LT06 classification of radio sources in NGC 253: S = Supernova Remnant; T = Thermally dominated H II region.

From the radio spectra, LT06 deduced that eight<sup>9</sup> of the 20 sources were thermally dominated H II regions (indicated with a flat intrinsic spectrum,  $\alpha > -0.4$ ) and the remaining 12 were consistent with steep intrinsic power-law spectra typical of

RSNe or SNRs. We find no difference in the source classification in our study.

The flux density for the sources with spectra consistent with RSNe or SNRs ranges from 2 to 30 mJy at 5 GHz. The relationship between the rise time and peak luminosity for core-collapse supernovae by Chevalier et al. (2006) predicts a rise time  $\leq 110$  days. A typical RSN follows a power-law decay

<sup>9</sup> A typographical error was made in Table 3 of LT06. The spectral index of 5.805-38.92 should be  $-1.20$  and not  $1.20$ .

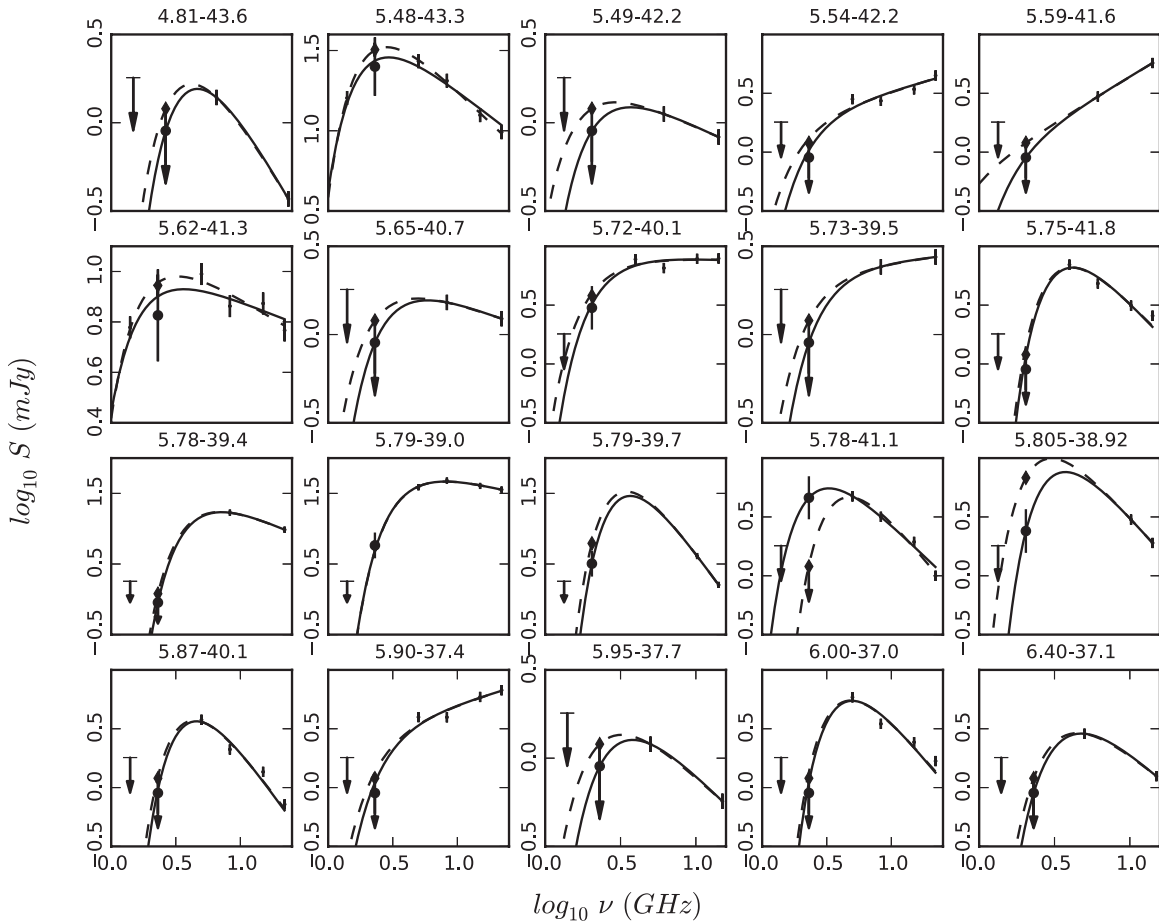


**Figure 7.** Measured flux densities (symbols with error bars) and free-free absorption models (lines) for 20 UA97 sources. The solid lines plot the free-free model derived using the 2008 2.3 GHz flux density values (star points). For comparison the free-free model derived with LT06’s 2004 2.3 GHz flux density values (dashed lines) are included. The  $3\sigma$  and  $5\sigma$  upper limits are shown for sources not detected at 1.4 GHz (1.8 mJy) and 2.3 GHz (1.2 mJy [2004] and 0.9 mJy [2008]).

that begins after this fast rise, and would be detectable over many years. However, no such decay has been observed for these compact sources over two decades, suggesting that they are probably very old SNRs.

### 3.2. The Supernova Remnant 5.48-43.3

#### 3.2.1. Morphology and Small-scale Features

The brightest source in NGC 253 at 2.3 GHz, 5.48-43.3, is the only fully resolved SNR in the starburst galaxy with the full LBA array (i.e., including the long baselines of Cd and Ho). In Figure 8 we present the two high-sensitivity VLBI images of 5.48-43.3 (the 2004 and 2008 epochs), restored with a beam size of  $13 \times 15$  mas and beam position angle of  $58^\circ$ . The contours were chosen to represent identical surface brightness levels in both images.

As first noted by LT06, 5.48-43.3 appears to be a shell-type SNR, with a diameter of  $\sim 70$ – $90$  mas (1.4–1.8 pc). At both epochs, the structure of 5.48-43.3 is dominated by the eastern lobe, which has a higher flux density than the western lobe by a factor of three. This may be the result of interactions with a denser interstellar medium in the direction of the eastern lobe.

Comparing the epochs, we notice that there are several differences in the lobes. Such apparent changes in the small scale structures are possibly due to ambiguities caused by the combination of structural evolution and image fidelity limitations, resulting from incomplete sampling of the *uv*

plane. The effects of *uv*-plane sampling on the appearance and evolution of complex small-scale structures, within spherically symmetric shell-like sources, are well documented by Heywood et al. (2009); they demonstrated that sparse *uv*-plane sampling, and the non-uniqueness of deconvolution, can add complex azimuthal structure to a radio brightness distribution that is in reality morphologically simple.

One striking feature of the Heywood et al. (2009) results is the departure from a spherically symmetric shell to a two-lobed structure (similar to SN 1987A (Ng et al. 2011) and 5.48-43.3) when the *uv*-plane coverage lacks intermediate baselines, similar to the *uv* coverage of both the 2004 (see Figure 2 of LT06) and the 2008 (Figure 1) observations. Thus, it is possible that 5.48-43.3 possesses a spherically symmetric (or slightly elliptical) morphology that is not recovered due to low sensitivity associated with sparse sampling of the *uv* plane. This effect is noticeable in the epochs without the intermediate baselines to Tidbinbilla (2006 and 2007), with the non-detection of the weaker, western lobe.

#### 3.2.2. Expansion of 5.48-43.3

With multiple high-resolution observations at the same frequency, it may be possible to determine the expansion speed of 5.48-43.3. In order to carry out such measurements, we use the AIPS task IRING to measure radial profiles (averaged in azimuth) of the source at each epoch. This method has been

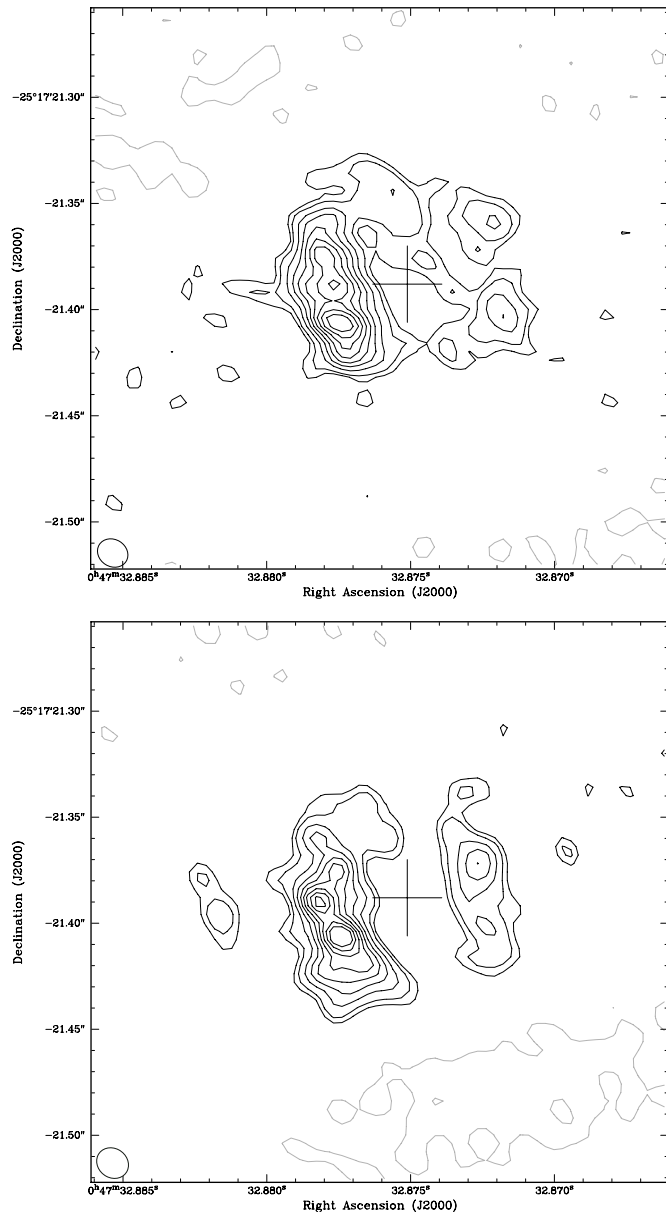


**Figure 8.** LBA images of 5.48-43.3 at 2.3 GHz taken from 2004 April 16/17 (top plot) from LT06 and 2008 June 5/6 (lower plot). The contours in both images correspond to  $-15\%$ ,  $15\%$ ,  $20\%$ ,  $30\%$ ,  $40\%$ ,  $50\%$ ,  $60\%$ ,  $70\%$ ,  $80\%$ , and  $90\%$  of the 2004 peak ( $2.4 \text{ mJy beam}^{-1}$ ). Both images are restored with the same beam,  $13 \times 15 \text{ mas}$  with a position angle of  $58^\circ$ . The cross indicates the assumed source center used to obtain the radial flux profile in Figure 9.

successfully implemented to determine the expansion speed of resolved SNRs in M82 (Beswick et al. 2006; Fenech et al. 2010). Owing to differences in the small-scale structure between the two epochs (as discussed in the previous section), determination of the geometrical center of 5.48-43.3 is difficult. To account for any positional offset between the epochs, the position of the peak surface brightness in the 2008 image was aligned to the position of the 2004 peak surface brightness, using the AIPS task OGEOM. A common geometrical center for both images was estimated by visual inspection, and indicated by the crosses in Figure 8. Using this position as the reference point, the radial profiles were obtained by measuring the integrated flux density within a series of 4 mas thick annuli, and are plotted in Figure 9. No discernible expansion between the two epochs can be seen in Figure 9. At the smaller radii, higher integrated flux densities

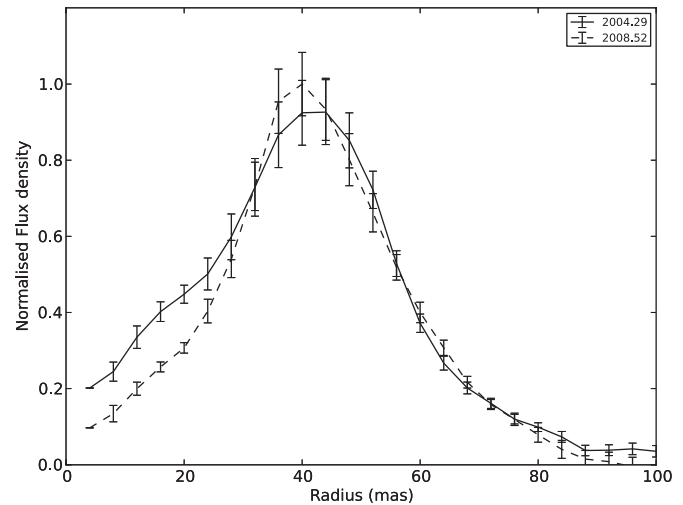


**Figure 9.** Radial flux density profile of the SNR 5.48-43.3 for the 2004 (solid line) and 2008 (dashed line) observations.

were recovered for the 2004 image. This is possibly due to differences in the short spacings of the  $uv$  coverages and/or deeper cleaning in the 2008 image.

If we consider an upper limit of the expansion speed on  $v = 10^4 \text{ km s}^{-1}$  (Beswick et al. 2006; Fenech et al. 2010) for SNRs in NGC 253, an expansion of  $\sim 2.2 \text{ mas}$ ,  $\sim 15\%$  of the 2.3 GHz LBA beam, is expected for 5.48-43.3 over 4.3 yr between the 2004 and 2008 LBA observations. To measure the expansion of 5.48-43.3, multiple observations separated by  $>10 \text{ yr}$  with the current LBA baselines, or observations with longer baselines ( $>3000 \text{ km}$ ) separated by  $>5 \text{ yr}$  would be needed.

### 3.3. The Supernova Rate in NGC 253

#### 3.3.1. Lower Limit Estimation

A lower limit on the supernova rate can be estimated based on the number of detected SNRs, their size, and an assumed expansion rate (LT06). Based upon the method by Ulvestad & Antonucci (1994) and an assumed radial expansion rate of  $10^4 \text{ km s}^{-1}$ , LT06 estimated the lower limit of the supernova rate to be  $0.14(v/10^4 \text{ km s}^{-1})$ . Our results from Section 3.2 are consistent with this as the minimum supernova rate.

#### 3.3.2. Previous Estimates of the Supernova Rate Upper Limit

No new sources have been detected in NGC 253 after two decades of multi-wavelength, high-resolution radio observations. The consequences of the non-detections for estimates of the supernova rate were first investigated by Ulvestad & Antonucci (1991, hereafter UA91). They assumed a hypothetical population of RSNe whose flux densities at 5 GHz peak 100 days after the optical maxima and decay as the  $-0.7$  power of time (Weiler et al. 1986, 1989). The RSN population was assumed to have peak luminosities uniformly distributed between 5 and 20 times that of Cas A, and an NGC 253 distance of 2.5 Mpc (TH85) was also assumed. UA91 found that  $\sim 2/3$  of the RSNe that occurred during the 18 month period between two 5 GHz epochs should be detectable above the second epoch's sensitivity limit. By assuming the events are Poisson distributed in time, UA91 determined with 95% confidence an upper limit to the supernova rate of  $3.0 \text{ yr}^{-1}$  in NGC 253. This model was used to estimate the supernova rate upper limit for two subsequent 5 GHz epochs,  $\sim 1.4 \text{ yr}^{-1}$  for a third epoch 2.5 yr later

**Table 5**  
Summary of Input Parameters to Different Supernova  
Rate Models of NGC 253

Input Parameters	UA <sup>a</sup>	LT06	This Paper
No. of epochs	4	6	11
$\Delta F^b$	$\mathcal{U}(5, 20)^c$	$\mathcal{U}(5, 20)$	Log-Gaussian
Frequency, $\nu$ (GHz)	5	2.3 and 5	2.3, 5, 8.3, 15, and 23
$T_r^d$ (days)	100	200 and 100	200, 100, 100, 70, and 50
$\beta^e$	-0.7	-0.7	-0.7
Spectral index, $\alpha$	...	0	Time-dependent <sup>f</sup>
$\tau_0^g$	...	6 <sup>h</sup>	6
Distance (Mpc)	2.55	3.94	3.44

#### Notes.

<sup>a</sup> Ulvestad & Antonucci (1991, 1994, 1997).

<sup>b</sup> Type II supernova peak luminosity distribution in units of Cas A luminosity at 5 GHz =  $7.34 \times 10^{24}$  erg s<sup>-1</sup> Hz<sup>-1</sup>.

<sup>c</sup>  $\mathcal{U}(a, b)$  means a uniform distribution with limits,  $a$  and  $b$ .

<sup>d</sup> Time after optical peak to reach radio peak luminosity at  $\nu$  GHz listed above.

<sup>e</sup> RSN luminosity decay with time (Weiler et al. 1986, 1989).

<sup>f</sup>  $\alpha_{2.3}^5$  from Weiler et al. (1986),  $\alpha_{5}^{23}$  from Weiler et al. (2007).

<sup>g</sup> Free-free optical depth at 1 GHz.

<sup>h</sup> Median value based upon the results of LT06.

(Ulvestad & Antonucci 1994) and  $\sim 0.3$  yr<sup>-1</sup> for a fourth epoch, 4.0 yr later (UA97).

With new distance measurements for NGC 253 ( $3.94 \pm 0.5$  Mpc; Karachentsev et al. 2003) and two additional high resolution observations, LT06 developed a new model based on the principles of UA91 and using new data: a 5 GHz<sup>10</sup> VLA observation by Mohan et al. (2005) and a 2.3 GHz LBA observation by LT06. The RSNe at 2.3 GHz were assumed to peak 200 days after the optical maxima at the same flux density as at 5 GHz (see Weiler et al. 1986). LT06 also considered the effects of free-free absorption by adjusting the flux densities of the RSNe with Equation (1), assuming a median value of  $\tau_0 = 6$ . The number of RSNe that occur between epochs was determined via a Poisson-distributed random number, given a specified supernova rate. The radio luminosities of the RSNe were allowed to evolve using the parametric equation of Weiler et al. (1986) into SNRs and then, given the time and sensitivity of the observation, a test was made to determine if each SNR could be detected. A Monte Carlo simulation was used to drive the model ( $\sim 10,000$  iterations), where the proportion of SNRs detected,  $\beta_{SN}$ , at the end of each epoch was obtained. The simulation was seeded with an initial supernova rate of  $0.1$  yr<sup>-1</sup> producing a confidence level for the  $\beta_{SN}$  at each epoch. Using linear interpolation, the supernova rate required to drive the simulation to a 95% confidence limit was determined and the simulation was repeated until the confidence limit was achieved. The resulting supernova rate was then used to seed the next epoch and the process was continued until all epochs were processed.

Using this model, LT06 found that the increased distance, combined with the effects of free-free absorption, decreased  $\beta_{SN}$  which resulted in an upper limit of the supernova rate at the end of the final epoch of  $2.4$  yr<sup>-1</sup>. A summary of the model parameters used by Ulvestad & Antonucci (1991, 1994, 1997) and LT06 to derive upper limits on the supernova rate are listed in Table 5.

<sup>10</sup> LT06 erroneously lists a 5.0 GHz observation in place of the 8.3 GHz observation by Mohan et al. (2005).

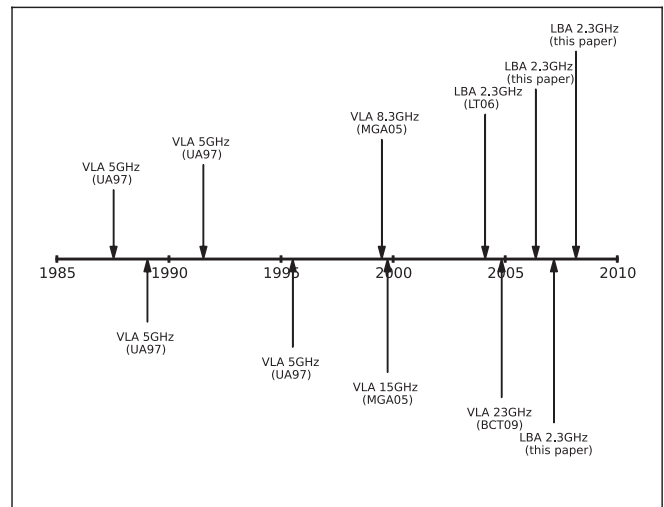


**Figure 10.** Timeline of observations used to estimate the upper limits on the supernova rate in NGC 253 by Ulvestad & Antonucci (1991, 1994, 1997), LT06, and this paper. The new observations introduced in the model by this paper are the VLA 8.3 GHz and 15 GHz (MGA05), VLA 23 GHz (BCT09), and three LBA 2.3 GHz (this paper) observations. Note: MGA05 - Mohan et al. (2005); BCT09 - Brunthaler et al. (2009a).

#### 3.3.3. Determining a New Supernova Rate Upper Limit

With additional high-resolution radio observations of NGC 253 since LT06, improved distance measurements to NGC 253, and availability of a more realistic RSN luminosity function (Lien et al. 2011), it is worth revisiting the estimates of the upper limit on the supernova rate. The additional NGC 253 observations are the three new 2.3 GHz LBA observations in this paper, plus 23 GHz VLA observations by Brunthaler et al. (2009a) and a 15 GHz VLA observation by Mohan et al. (2005). Figure 10 gives a timeline of all observations of NGC 253 used to determine the supernova rate. To further constrain the upper limit on the supernova rate with these observations, we have developed a new model based on the principles of Ulvestad & Antonucci (1991) and LT06, as well as incorporating suggested improvements by LT06.

*Improved core-collapse supernova peak luminosity distribution.* At 5 GHz and 2.3 GHz our hypothetical RSN is the same as that used by UA91 and LT06 (see the previous section and Table 5). At 8.3 GHz, 15 GHz, and 23 GHz we assume that the RSN luminosity peaks 100, 70, and 50 days after the optical maximum at the same luminosity as at 5 GHz. This assumption closely agrees with the light curves of SN 1993J (Weiler et al. 2007).

In the models of UA91 and LT06, the distribution of the 5 GHz peak luminosities of RSNe was assumed to be uniformly distributed between 5 and 20 times the luminosity of Cas A. This assumption follows Weiler et al. (1989), who came to this conclusion after comparing the peak flux densities at 5 GHz of 16 Type II supernovae (three detections and 13 upper limits). Since the study by Weiler et al. (1989) there have been many more new detections of Type II as well as Type Ib supernovae in the radio. Thus it is worth re-investigating the 5 GHz peak luminosity distribution of these objects.

Table 6 lists 51 core-collapse (29 Type II and 22 Type Ib) supernovae whose 5 GHz peak flux density have either been detected or estimated via spectral index<sup>11</sup> or extrapolation using

<sup>11</sup> For peak flux densities detected at 8.4 GHz, a spectral index of 0 is assumed, following SN1993J (Weiler et al. 2007).

**Table 6**  
Observed 5 GHz Peak Flux Density of Core-collapse Supernovae

Name	Galaxy	Type	Distance <sup>a</sup> (Mpc)	Detected? <sup>b</sup>	$S_5^c$ (mJy)	$L_6^d$	$L_{5,\text{CasA}}^e$	Ref.
SN1983N	M83	Ibc	4.5	D	40.10	9.72	132.45	1
SN1984L	NGC 4991	Ibc	21.7	D	4.59	25.86	352.54	2
SN1990B	NGC 4568	Ibc	18.2	D	1.26	4.99	68.08	3
SN1994I	M51	Ibc	8.0	D	16.20	12.50	170.38	4
SN1998bw	ESO184-G082	Ibc	37.3	D	37.40	622.59	8487.24	5
SN2000C	NGC 2415	Ibc	59.0	E	0.19	7.79	106.18	6
SN2001B	IC391	Ibc	24.0	D	2.56	17.64	240.51	6
SN2001ci	NGC 3079	Ibc	17.0	D	1.06	3.67	50.06	6
SN2002ap	NGC 628	Ibc	7.3	D	0.45	0.29	3.94	7
SN2002cj	ESO582-G5	Ibc	106.0	D	0.22	29.58	403.19	6
SN2002dg	Anon.	Ibc	215.0	E	0.09	50.88	693.65	6
SN2003L	NGC 3506	Ibc	92.0	D	2.56	258.75	3527.31	8
SN2003bg	MCG-05-10-15	Ibc	19.6	D	52.81	242.74	3309.07	9
SN2004cc	NGC 4568	Ibc	18.0	E	3.26	12.64	172.28	10
SN2004dk	NGC 6118	Ibc	23.0	D	1.80	11.39	155.31	10
SN2004gq	NGC 1832	Ibc	26.0	D	5.75	46.51	634.00	10
SN2007bg	Anon.	Ibc	152.0	D	1.10	304.91	4156.62	11
SN2007gr	NGC 1058	Ibc	7.7	D	1.00	0.71	9.67	12
SN2008D	NGC 2770	Ibc	27.0	E	3.00	26.17	356.72	13
SN2009bb	NGC 3278	Ibc	40.0	D	12.00	229.73	3131.69	14
SN2010as	NGC 6000	Ibc	27.3	D	1.40	12.48	170.19	15
PTF11qej	SDSS <sup>f</sup>	Ib	124.0	D	5.43	998.98	13618.22	16
SN1970g	NGC 5457	II	7.2	D	2.50	1.55	21.14	17
SN1974E	NGC 4038	II?	20.9	D	1.24	6.48	88.35	18
SN1978K	NGC 1313	II	4.1	D	518.00	104.19	1420.28	18
SN1979C	NGC 4321	IIL	22.0	D	12.40	71.81	978.91	18
SN1980K	NGC 6946	IIL	7.0	D	2.45	1.44	19.58	18
SN1981k	NGC 4258	II	6.6	D	5.15	2.68	36.59	18
SN1982aa	NGC 6052	II	66.0	D	19.10	995.48	13570.58	18,19
SN1985L	NGC 5033	II	12.9	D	1.56	3.11	42.34	20
SN1986E	NGC 4302	II	16.8	D	0.33	1.11	15.19	21
SN1986J	NGC 891	IIn	12.0	D	135.00	232.60	3170.83	18
SN1988Z	MCG+03-28-022	IIP	94.5	D	1.85	197.67	2694.71	22
SN1993J	M81	IIB	3.6	D	96.90	15.28	208.26	23
SN1995N	MCG-02-38-17	IIn	24.0	E	9.00	62.03	845.56	24
SN1997eg	NGC 5012	II	40.0	E	10.00	191.44	2609.74	25
SN1998S	NGC 3877	II	17.0	E	1.04	3.60	49.02	26
SN1999em	NGC 1637	II	7.8	E	0.30	0.22	2.98	26
SN2000ft	NGC 7469	II?	70.0	D	1.76	103.30	1408.25	27
SN2001ig	NGC 7424	IIB	11.5	D	21.90	34.65	472.41	28
SN2001gd	NGC 5033	IIB	20.0	D	7.96	38.10	519.34	29
SN2004dj	NGC 2403	IIP	3.6	E	1.90	0.29	4.02	30
SN2004et	NGC 6946	II	5.5	E	2.50	0.90	12.34	31
SN2006jd	UGC 4179	IIB	76.8	D	2.22	156.39	2131.91	32
SN2008ax	NGC 4490	IIP	8.1	D	4.00	3.13	42.70	33
SN2008iz	M82	II	3.2	E	180.00	22.05	300.64	34
SN2011cb	PGC 69707	IIB	29.2	D	0.73	7.46	101.73	35
SN2011dh	M51	IIP	8.0	D	7.80	6.02	82.04	36
SN2011ei	NGC 6925	IIB	28.5	D	0.56	5.48	74.72	37
A25	Arp220	IIP	44.8	E	0.30	7.20	98.21	38
A27	Arp220	IIP?	44.8	E	0.75	18.01	245.52	38

**Notes.**<sup>a</sup> Estimated from the NASA/IPAC Extragalactic Database (NED), where appropriate.<sup>b</sup> D—peak flux detected at 5 GHz; E—peak flux at 5 GHz estimated.<sup>c</sup> Peak Flux Density at 5 GHz.<sup>d</sup> Peak luminosity at 5 GHz; units =  $10^{26}$  erg s<sup>-1</sup> Hz<sup>-1</sup>.<sup>e</sup> Luminosity ratio to Cassiopeia A (Cas A) 5 GHz peak luminosity:  $7.34 \times 10^{24}$  erg s<sup>-1</sup> Hz<sup>-1</sup>.<sup>f</sup> SDSS J131341.57+471757.2.

**References.** (1) Sramek et al. 1984; (2) Weiler et al. 1986; (3) van Dyk et al. 1993; (4) Weiler et al. 2011; (5) Kulkarni et al. 1998; (6) Berger et al. 2003; (7) Berger et al. 2002; (8) Soderberg et al. 2005; (9) Soderberg et al. 2006a; (10) Wellons et al. 2012; (11) Salas et al. 2013; (12) Soderberg et al. 2010; (13) Soderberg et al. 2008; (14) Bietenholz et al. 2010; (15) Ryder et al. 2010a; (16) Corsi et al. 2013; (17) Weiler et al. 1989; (18) Weiler et al. 2002; (19) Metcalfe et al. 2005; (20) van Dyk et al. 1998; (21) Montes et al. 1997; (22) Williams et al. 2002; (23) Weiler et al. 2007; (24) Chandra et al. 2009; (25) Lacey et al. 1998; (26) Pooley et al. 2002; (27) Pérez-Torres et al. 2009; (28) Ryder et al. 2004; (29) Stockdale et al. 2007; (30) Beswick et al. 2005; (31) Argo et al. 2005; (32) Chandra et al. 2012; (33) Roming et al. 2009; (34) Gendre et al. 2013; (35) Krauss et al. 2012; (36) Ryder et al. 2011a; (37) Milišavljević et al. 2013; (38) Bondi et al. 2012.

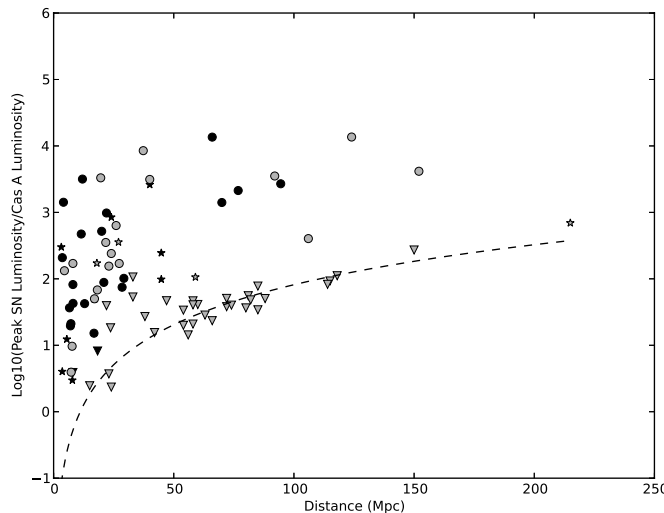


**Figure 11.** 5 GHz peak luminosity ratio to Cas A as a function of distance for Type II supernovae (black points) and Type Ibc supernovae (gray points). The circles and stars are supernovae with detected and estimated peak luminosities (29 Type II and 22 Type Ibc, see Table 6). The upside-down triangles are supernovae whose peak luminosities have not been detected (2 Type II and 32 Type Ibc, see Table 7). The dashed line is the average  $3\sigma$  detection limit of the VLA from Berger et al. (2003).

the models by Chevalier (1982) or Weiler et al. (2002). This table is represented graphically in Figure 11, where the Type Ibc (gray symbols) and Type II (black symbols) luminosity ratio to Cas A's at 5 GHz is plotted on the y-axis and their distances on the x-axis. Included in the plots are the 5 GHz peak luminosity upper limits for 34 core-collapse supernovae not detected in the radio (Table 7), that follow the average  $3\sigma$  detection limit of the VLA (the dashed lines; from Berger et al. 2003). Using the detected core-collapse supernovae listed in Table 6, we derived a more accurate luminosity distribution at 5 GHz shown in Figure 12. The data are divided into bins of size  $\Delta \log_{10}(L_{5,\text{CasA}})$ <sup>12</sup> = 1. The dashed line presents the best fit Gaussian with a mean luminosity ratio of 245.5, standard deviation of 1.27, and  $\chi^2 = 0.018$ . This distribution is similar to that presented by Lien et al. (2011).

However, this analysis ignores the upper limits (Table 7) entirely, and so we should consider whether these offer any significant additional information. While their true luminosities are unknown, we need to determine if, given the upper limits, these supernovae are distributed differently to Figure 12. To examine this we calculate the probability (or  $p$ -value), using the cumulative distribution function derived from the Gaussian distribution in Figure 12, that a supernova will have a luminosity less than the upper limits listed in Table 7. The  $p$ -values (Table 7), although on average are lower than 0.5, are probably consistent with the chosen luminosity function given that the upper limits may not have been observed at a time corresponding to when the peak flux density actually occurs. However, detailed work on testing whether the upper limits in Table 7 are consistent with the chosen model are beyond the scope of this paper.

*Improved spectral indices.* Weiler et al. (1986, 2007) showed that the spectral index between 6 cm and 20 cm evolves with time for a number of RSNe. This has also been shown to be true for SN 1993J for wavelength pairs of 1.2/2 cm, 2/3.6 cm, and 3.6/6 cm (Weiler et al. 2007). Thus, it is expected that 2.3/5 GHz, 5/8.3 GHz, 5/15 GHz, and 5/23 GHz spectral indices will display similar variations with time. To account for

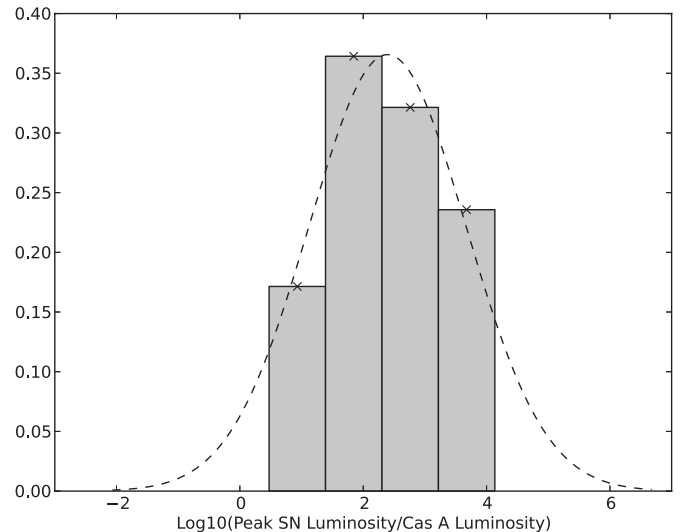


**Figure 12.** Normalized radio luminosity distribution at 5 GHz of 51 core-collapse supernovae as a function of  $\log_{10}(L_{5,\text{CasA}})$ . The x-axis mirrors the y-axis of Figure 11 and is given in Table 6. The data are binned to  $\Delta \log_{10}(L_{5,\text{CasA}}) = 1$ . The dashed curve shows a non-linear least-squares fitted Gaussian to the underlying data (black x's). The resulting fit: mean  $\log_{10}(L_{5,\text{CasA}}) = 2.39$ ,  $\sigma = 1.27$ , and  $\chi^2 = 0.018$ .

this, we have included light curves that best describe the spectral indices between 6 and 20 cm from SN 1980k (Weiler et al. 1986) and between 6 and 3.6 cm, 6 and 2 cm, and 6 and 1.2 cm from SN 1993J (Weiler et al. 2007).

*The new supernova rate upper limit.* Table 8 lists the results of applying the improved model parameters described above and listed in Column 4 of Table 5, to the Monte Carlo simulation of LT06 (see Section 3.3.2). We find that the proportion of SNRs detected,  $\beta_{\text{SN}}$ , at the end of each epoch is relatively consistent, with minor variations between 0.66 and 0.84. The major changes occur during epochs where the sensitivity varies by almost an order of magnitude. The consistently high  $\beta_{\text{SN}}$  resulted in an upper limit on the supernova rate of  $v_{\text{SN}} = 0.2 \text{ yr}^{-1}$  at the end of the final epoch. The results of the simulation indicate that the radio observations are detecting 60%–80% of all SNRs in NGC 253, thus pointing to the existence of a small population of undetected SNRs. Moreover, the fact that no RSN or SNR has been observed in NGC 253 during 21 yr of radio observation suggests a low rate of RSN production in NGC 253.

The final result for  $v_{\text{SN}}$  agrees with estimates determined from near infrared (NIR) observations of the [Fe II] line ( $0.24 \text{ yr}^{-1}$ ) by Rosenberg et al. (2013). Observations of the [Fe II] line have been shown to be a strong tracer of shocks associated with SNRs (Rosenberg et al. 2012, 2013). Dust grains in the interstellar medium containing Fe atoms are destroyed via the shocks. The process releases the Fe atoms, which are then ionized by the interstellar radiation field. In the post shock region, Fe<sup>+</sup> is excited by electron collisions, causing it to emit at NIR wavelengths. However, there are possible contributions to the [Fe II] line from shocks due to other processes such as mergers (Rosenberg et al. 2012). Thus, it is possible that the NIR [Fe II] observations are overestimating the supernova rate upper limit.

The major uncertainty in our model arises from the RSN peak luminosity distribution. First, the detection of RSNe has primarily been through follow-up observations of optical supernovae, resulting in a small and incomplete sample whose luminosity depends on the sensitivity of the survey. Second, there is the possibility that many RSNe are not visible in the

<sup>12</sup>  $L_{5,\text{CasA}}$  is the RSN 5 GHz peak luminosity ratio to Cas A's.

**Table 7**  
Peak Flux Density Upper Limits of Undetected Core-collapse Supernova at 5 GHz

Name	Galaxy	Type	Distance (Mpc)	$S_5$ (mJy)	$L_5$	$L_{5;\text{CasA}}$	p-value <sup>a</sup>	Ref.
SN1980I	NGC 4374	Ibc	22.0	<0.50	<2.90	<39.47	0.27	1,2
SN1980N	NGC 1316	Ibc	33.0	<0.60	<7.82	<106.58	0.39	1
SN1981B	NGC 4536	Ibc	33.0	<0.30	<3.91	<53.29	0.30	1
SN1999ex	IC 5179	Ibc	54.0	<0.07	<2.48	<33.77	0.25	3
SN2000cr	NGC 5395	Ibc	54.0	<0.04	<1.47	<19.98	0.20	3
SN2000ew	NGC 3810	Ibc	15.0	<0.07	<0.18	<2.46	0.06	3
SN2000fn	NGC 2526	Ibc	72.0	<0.05	<2.79	<38.05	0.26	3
SN2001M	NGC 3240	Ibc	56.0	<0.03	<1.05	<14.32	0.17	3
SN2001ai	NGC 5278	Ibc	118.0	<0.05	<8.16	<111.29	0.39	3
SN2001bb	IC 4319	Ibc	72.0	<0.06	<3.72	<50.73	0.29	3
SN2001ef	IC 381	Ibc	38.0	<0.12	<1.99	<27.09	0.23	3
SN2001ej	UGC 3829	Ibc	63.0	<0.04	<2.09	<28.48	0.23	3
SN2001is	NGC 1961	Ibc	60.0	<0.07	<3.02	<41.10	0.27	3
SN2002J	NGC 3464	Ibc	58.0	<0.09	<3.42	<46.64	0.28	3
SN2002bl	UGC 5499	Ibc	74.0	<0.05	<2.95	<40.19	0.27	3
SN2002bm	MCG013219	Ibc	85.0	<0.07	<5.71	<77.78	0.35	3
SN2002cg	UGC 10415	Ibc	150.0	<0.07	<19.92	<271.58	0.51	3
SN2002cp	NGC 3074	Ibc	80.0	<0.04	<2.68	<36.54	0.26	3
SN2002dn	IC 5145	Ibc	115.0	<0.04	<6.80	<92.76	0.37	3
SN2002ge	NGC 7400	Ibc	47.0	<0.13	<3.44	<46.84	0.29	3
SN2002gy	UGC 2701	Ibc	114.0	<0.04	<6.06	<82.67	0.35	3
SN2002hf	MCG05320	Ibc	88.0	<0.04	<3.71	<50.52	0.29	3
SN2002hn	NGC 2532	Ibc	82.0	<0.04	<3.54	<48.26	0.29	3
SN2002ho	NGC 4210	Ibc	42.0	<0.05	<1.14	<15.54	0.17	3
SN2002hy	NGC 3464	Ibc	58.0	<0.07	<2.98	<40.60	0.27	3
SN2002hz	UGC 12044	Ibc	85.0	<0.03	<2.51	<34.18	0.25	3
SN2002ji	NGC 3655	Ibc	23.0	<0.04	<0.27	<3.71	0.08	3
SN2002jj	IC 340	Ibc	66.0	<0.03	<1.72	<23.45	0.21	2
SN2002jp	NGC 3313	Ibc	58.0	<0.04	<1.53	<20.85	0.20	3
SN2002jz	UGC 2984	Ibc	24.0	<0.03	<0.17	<2.35	0.06	3
SN2003jd	MCG0159021	Ibc	81.0	<0.05	<4.08	<55.65	0.31	4
SN2011hp	NGC 4219	Ibc	23.7	<0.20	<1.34	<18.32	0.19	5
SN2005cs	M51	II	8.0	<0.37	<0.29	<3.89	0.08	6
SN2009mk	PGC 474	IIb	18.3	<0.15	<0.60	<8.19	0.12	7

**Notes.** Where appropriate, symbols and headings have same meaning as Table 6. Note: Only core-collapse supernovae that were observed in the radio within 200 days of the optical maximum are selected.

<sup>a</sup> The probability the supernova's peak radio luminosity is actually less than the observed upper limits given the cumulative distribution function derived from Figure 12.

**References.** (1) Weiler et al. 1989; (2) Weiler et al. 1986; (3) Berger et al. 2003; (4) Soderberg et al. 2006b; (5) Ryder et al. 2011b; (6) Stockdale et al. 2005; (7) Ryder et al. 2010b.

optical due to extinction and we may be looking at a slightly different sub-population.

Further uncertainty comes from the assumed rise time of the RSNe at the different frequencies. In this model, for simplicity, constant rise times (the time to reach maximum radio luminosities) were assumed for the hypothetical RSNe at the different frequencies. However, this has been observed to be variable for different RSNe (e.g., Weiler et al. 1986, 2002). Additionally, the relation between the rise time and peak luminosity has also been observed to be variable (Chevalier et al. 2006) and does not necessarily follow a one-to-one relationship as assumed in the model presented.

Further refinement to the supernova rate of NGC 253 could be obtained from either a large unbiased sample of the peak flux densities of RSNe, or direct observations of the RSN population in NGC 253. Both possibilities can be provided by the Square Kilometer Array<sup>13</sup> (SKA) and new generation telescopes, such

as the Karl G. Jansky VLA<sup>14</sup> (JVLA). The sensitivity of both instruments may provide the opportunity to detect a population of weak SNRs that are faint due to either free-free absorption or intrinsic properties. The SKA is expected to have a Type II supernova detection rate of  $\sim 620 \text{ yr}^{-1} \text{ deg}^{-2}$  out to a redshift  $z \sim 5$  (Lien et al. 2011). The JVLA and precursors to the SKA may provide a detection rate of  $\sim 160 \text{ yr}^{-1} \text{ deg}^{-2}$  out to redshift  $z \sim 3$  (Lien et al. 2011).

### 3.4. Star Formation Rate

With new upper limits on the supernova rate, we can provide a new estimate for the SFR in NGC 253. Following Condon (1992), the SFR can be determined directly from the supernova rate (and vice versa). By assuming that all stars with mass  $> 8 M_\odot$  eventually form supernovae, the relation between SFR

<sup>13</sup> <http://www.skatelescope.org/>

<sup>14</sup> <https://science.nrao.edu/facilities/vla>

**Table 8**  
Supernova Rate Upper Limits from Monte Carlo Simulations

Epoch	Time <sup>a</sup> (yr)	$\nu^b$ (GHz)	Sensitivity <sup>c</sup> (mJy)	$\beta_{SN}^d$ -	$\nu_{SN}^e$ ( $\text{yr}^{-1}$ )
1	...	5.0	...	...	<2.71
2	1.5	5.0	3.0	0.746	<1.04
3	2.5	5.0	3.0	0.713	<0.53
4	4.0	5.0	3.0	0.683	<0.34
5	4.0	8.3	0.3	0.803	<0.33
6	0.25	15	0.6	0.838	<0.25
7	4.5	2.3	1.2	0.697	<0.24
8	0.5	23	2.0	0.661	<0.22
9	1.7	2.3	2.0	0.676	<0.21
10	0.8	2.3	2.2	0.689	<0.20
11	1.0	2.3	0.9	0.791	<0.20

**Notes.**<sup>a</sup> Time between epochs.<sup>b</sup> Observed frequency.<sup>c</sup> The  $5\sigma$  sensitivity of the observations.<sup>d</sup> Proportion of RSNe detected at the end of each epoch.<sup>e</sup> Supernova rate based upon all observations prior to and including that epoch.

and the supernova rate is given by:

$$\left[ \frac{\text{SFR}(M \geq 5 M_\odot)}{M_\odot \text{ yr}^{-1}} \right] = 24.4 \left[ \frac{\nu_{SN}}{\text{yr}^{-1}} \right]. \quad (3)$$

Using the new supernova rate upper limits of  $\nu_{SN} < 0.2 \text{ yr}^{-1}$  (Section 3.3), we find  $\text{SFR}(M \geq 5 M_\odot) < 4.9 M_\odot \text{ yr}^{-1}$ . We can compare this upper limit to estimates from independent methods. If one assumes that the main contributions to the observed radio luminosity in a starburst are from RSNe, SNRs, and thermal H II regions, then the SFR of that region is directly proportional to its radio luminosity at the observed radio wavelength and can be calculated using the relation given by Condon (1992) and Haarsma et al. (2000). Ott et al. (2005) observed a total flux density of 0.59 Jy for NGC 253 at 24 GHz. Using the relation by Haarsma et al. (2000) and the data from Ott et al. (2005) we obtain  $\text{SFR}(M \geq 5 M_\odot) = 9.3 M_\odot \text{ yr}^{-1}$ . Additional observations of NGC 253 at 23 GHz (total flux density of 0.56 Jy) by Takano et al. (2005) give a similar  $\text{SFR}(M \geq 5 M_\odot) = 8.7 M_\odot \text{ yr}^{-1}$  for the  $\sim 300$  pc nuclear region, using the same method.

The  $\text{SFR}(M \geq 5 M_\odot)$  can also be determined from far infrared (FIR) emission using Equation (26) from Condon (1992). From FIR luminosity measurements with *IRAS*<sup>15</sup> (Radovich et al. 2001) and scaling for the new distance 3.44 Mpc, the SFR is  $1.3\text{--}2.0 M_\odot \text{ yr}^{-1}$  for the inner  $\sim 300$  pc nuclear region and  $2.6\text{--}3.2 M_\odot \text{ yr}^{-1}$  for the entire galaxy. FIR luminosity measurements of the inner  $\sim 350$  pc nuclear region by *Spitzer*<sup>16</sup> (Paglione & Abrahams 2012) lead to an estimate of  $2.7 M_\odot \text{ yr}^{-1}$ . It is encouraging that the  $\text{SFR}(M \geq 5 M_\odot)$  calculated using different estimators are in broad agreement with each other. However, the differences point to the existence of systematic or intrinsic differences between the different estimators.

The supernova rate derived from the FIR luminosity (via Equation (20) from Condon 1992) is  $0.05\text{--}0.13 \text{ yr}^{-1}$  and is similar to the lower limit of the supernova rate deduced from expansion rates (LT06).

**4. SUMMARY**

We have presented the results of multi-epoch observations of the southern starburst galaxy NGC 253 with the LBA at 2.3 GHz. The results presented here are complementary to previous 2.3 GHz LBA observations by Lenc & Tingay (2006). We find the following results.

1. Seven compact sources were detected in the highest sensitivity observation (the 2008 epoch). All sources were identified with higher-frequency VLA observations (UA97), while six were identified with 2.3 GHz LBA detections by LT06. The three brightest sources were also detected in the lower-sensitivity observations (2006 and 2007).
2. The shell-like SNR, 5.48-43.3, was successfully imaged with the highest resolution in all three epochs. The structure in the 2008 image shows a double-lobed morphology which is dominated by the eastern lobe. The weaker, western lobe was not detected in the 2006 and 2007 observations, which is attributed to lower sensitivity and fidelity, due to the lack of the 70 m Tidbinbilla antenna.
3. Observed differences in the small-scale structure of 5.48-43.3 between the 2004 (LT06) and the 2008 (this paper) observations can be explained by deconvolution errors associated with sparse  $uv$ -plane sampling. No discernible expansion has been observed for 5.48-43.3 between the 2004 and 2008 epochs.
4. The spectra of the 20 compact sources in NGC 253 from LT06 are compared with the spectra obtained with the new 2.3 GHz LBA flux density measurements (2008 epoch). As with LT06, we find that the spectra fit a free-free absorption model, with little difference in the spectra between the epochs.
5. Our results show no change in the classification of the compact sources by LT06. Out of 20 sources, 12 have steep spectra associated with SNRs, while the remaining eight have flat intrinsic power-law spectra ( $\alpha > 0.4$ ), indicative of H II regions.
6. We derive an improved RSN peak luminosity distribution at 5 GHz using data from the literature for 51 core-collapse supernovae (29 Type II and 22 Type Ibc).
7. We estimate a value for the upper limit of the supernova rate of  $0.2 \text{ yr}^{-1}$  for the inner 300 pc of NGC 253, using an improved model that is based upon the principles of UA91 and LT06. This result was found to be consistent with estimates from NIR observations.
8. The results of our model indicate that the radio observations are detecting 60%–80% of all SNRs in NGC 253, thus pointing to the existence of a small population of undetected SNRs. Moreover, no RSN or SNR has been observed in NGC 253 during 21 yr of radio observation, which suggests a low rate of RSN production in NGC 253.
9. A new upper limit to the star formation rate of  $\text{SFR}(M \geq 5 M_\odot) < 4.9 M_\odot \text{ yr}^{-1}$  is estimated directly from the supernova rate limits for the inner 300 pc region of the galaxy, which is consistent with independent estimates.

The International Centre for Radio Astronomy Research is a joint venture between Curtin University and the University of Western Australia, funded by the state government of Western Australia and the joint venture partners. The Long Baseline Array is part of the Australia Telescope which is funded by the Commonwealth of Australia for operation as a National Facility managed by CSIRO. S.J.T. is a Western Australian Premier's

<sup>15</sup> <http://irsa.ipac.caltech.edu/IRASdocs/exp.sup/ch1/index.html><sup>16</sup> <http://www.spitzer.caltech.edu/>

Research Fellow, funded by the state government of Western Australia. The Centre for All-sky Astrophysics (CAASTRO) is an Australian Research Council Centre of Excellence, funded by grant CE110001020. We wish to thank Paola Castangia & Andreas Brunthaler for use of their VLA data, Cormac Reynolds for assisting with the calibration of the LBA data, and Cath Trott for helpful discussions on statistics. This research has made use of material from the Bordeaux VLBI Image Database (BVID) and the NASA/IPAC Extragalactic Database (NED) which is operated by the Jet Propulsion Laboratory, California Institute of Technology, under contract with the National Aeronautics and Space Administration. We thank the anonymous referee for comments that improved this paper.

*Facilities:* ATCA, Mopra, Parkes, Ceduna Radio Observatory

## REFERENCES

- Antonucci, R. R. J., & Ulvestad, J. S. 1988, *ApJL*, **330**, L97  
 Argo, M. K., Beswick, R. J., Muxlow, T. W. B., et al. 2005, *MmSAI*, **76**, 565  
 Batejat, F., Conway, J. E., Rushton, A., Parra, R., et al. 2012, *A&A*, **542**, L24  
 Becker, R. H., White, R. L., & Helfand, D. J. 1995, *ApJ*, **450**, 559  
 Berger, E., Kulkarni, S. R., & Chevalier, R. A. 2002, *ApJL*, **577**, L5  
 Berger, E., Kulkarni, S. R., Frail, D. A., & Soderberg, A. M. 2003, *ApJ*, **599**, 40  
 Beswick, R. J., Muxlow, T. W. B., Argo, M. K., et al. 2005, *ApJL*, **623**, L21  
 Beswick, R. J., Riley, J. D., Martí-Vidal, I., et al. 2006, *MNRAS*, **369**, 1221  
 Bietenholz, M. F., Soderberg, A. M., Bartel, N., et al. 2010, *ApJ*, **725**, 4  
 Bondi, M., Pérez-Torres, M. A., Herrero-Illana, R., & Pérez-Torres Alberdi, A. 2012, *A&A*, **539**, A134  
 Brunthaler, A., Castangia, P., Tarchi, A., et al. 2009a, *A&A*, **497**, 103  
 Brunthaler, A., Menten, K. M., Reid, M. J., et al. 2009b, *A&A*, **499**, L17  
 Carilli, C. L. 1996, *A&A*, **305**, 402  
 Chandra, P., Chevalier, R. A., Chugai, N., et al. 2012, *ApJ*, **755**, 110  
 Chandra, P., Stockdale, C. J., Chevalier, R. A., et al. 2009, *ApJ*, **690**, 1839  
 Chevalier, R. A. 1982, *ApJ*, **259**, 302  
 Chevalier, R. A., Fransson, C., & Nymark, T. K. 2006, *ApJ*, **641**, 1029  
 Condon, J. J. 1992, *ARA&A*, **30**, 575  
 Corsi, A., Ofek, E. O., Gal-Yam, A., et al. 2013, arXiv:1307.2366  
 Dalcanton, J. J., Williams, B. F., Seth, A. C., et al. 2009, *ApJS*, **183**, 67  
 Deller, A. T., Brisken, W. F., Phillips, C. J., et al. 2011, *PASP*, **123**, 275  
 Deller, A. T., Tingay, S. J., Bailes, M., & West, C. 2007, *PASP*, **119**, 318  
 Fenech, D., Beswick, R., Muxlow, T. W. B., Pedlar, A., & Argo, M. K. 2010, *MNRAS*, **408**, 607  
 Ferreira, S. E. S., & de Jager, O. C. 2008, *A&A*, **478**, 17  
 Gendre, M. A., Fenech, D. M., Beswick, R. J., Muxlow, T. W. B., & Argo, M. K. 2013, *MNRAS*, **431**, 1107  
 Haarsma, D. B., Partridge, R. B., Windhorst, R. A., & Richards, E. A. 2000, *ApJ*, **544**, 641  
 Hales, C. A., Murphy, T., Curran, J. R., et al. 2012, *MNRAS*, **425**, 979  
 Heywood, I., Blundell, K. M., Klöckner, H.-R., & Beasley, A. J. 2009, *MNRAS*, **392**, 855  
 Karachentsev, I. D., Grebel, E. K., Sharina, M. E., et al. 2003, *A&A*, **404**, 93  
 Krauss, M. I., Soderberg, A. M., Chomiuk, L., et al. 2012, *ApJL*, **750**, L40  
 Kulkarni, S. R., Frail, D. A., Wieringa, M. H., et al. 1998, *Natur*, **395**, 663  
 Lacey, C. K., Weiler, K. W., Sramek, R. A., & van Dyk, S. D. 1998, *IAU Circ.*, **7068**, 2  
 Lehnert, M. D., & Heckman, T. M. 1996, *ApJ*, **472**, 546  
 Lenc, E., & Tingay, S. J. 2006, *AJ*, **132**, 1333  
 Lenc, E., & Tingay, S. J. 2009, *AJ*, **137**, 537  
 Lien, A., Chakraborty, N., Fields, B. D., & Kemball, A. 2011, *ApJ*, **740**, 23  
 Lonsdale, C. J., Diamond, P. J., Thrall, H., Smith, H. E., & Lonsdale, C. J. 2006, *ApJ*, **647**, 185  
 McDonald, A. R., Muxlow, T. W. B., Wills, K. A., et al. 2002, *MNRAS*, **334**, 912  
 Metcalfe, L., O'Halloran, B., McBreen, B., et al. 2005, *A&A*, **444**, 777  
 Milisavljevic, D., Margutti, R., Soderberg, A. M., et al. 2013, *ApJ*, **767**, 71  
 Mohan, N. R., Anantharamaiah, K. R., & Goss, W. M. 2002, *ApJ*, **574**, 701  
 Mohan, N. R., Goss, W. M., & Anantharamaiah, K. R. 2005, *A&A*, **432**, 1  
 Montes, M. J., van Dyk, S. D., Weiler, K. W., Sramek, R. A., & Panagia, N. 1997, *ApJL*, **482**, L61  
 Muxlow, T. W. B., Beswick, R. J., Garrington, S. T., et al. 2010, *MNRAS*, **404**, L109  
 Muxlow, T. W. B., Pedlar, A., Wilkinson, P. N., et al. 1994, *MNRAS*, **266**, 455  
 Ng, C.-Y., Potter, T. M., Staveley-Smith, L., et al. 2011, *ApJL*, **728**, L15  
 Ott, J., Weiss, A., Henkel, C., & Walter, F. 2005, *ApJ*, **629**, 76  
 Paglione, T. A. D., & Abrahams, R. D. 2012, *ApJ*, **755**, 10  
 Parra, R., Conway, J. E., Diamond, P. J., et al. 2007, *ApJ*, **659**, 314  
 Pedlar, A., Muxlow, T. W. B., Garrett, M. A., et al. 1999, *MNRAS*, **307**, 761  
 Pérez-Torres, M. A., Alberdi, A., Colina, L., et al. 2009, *MNRAS*, **399**, 1641  
 Pooley, D., Lewin, W. H. G., Fox, D. W., et al. 2002, *ApJ*, **572**, 932  
 Radovich, M., Kahapää, J., & Lemke, D. 2001, *A&A*, **377**, 73  
 Reynolds, J. 1994, CSIRO, ATNF Technical Memo, 39, 040  
 Romero-Cañizales, C., Mattila, S., Alberdi, A., et al. 2011, *MNRAS*, **415**, 2688  
 Roming, P. W. A., Pritchard, T. A., Brown, P. J., et al. 2009, *ApJL*, **704**, L118  
 Rosenberg, M. J. F., van der Werf, P. P., & Israel, F. P. 2012, *A&A*, **540**, A116  
 Rosenberg, M. J. F., van der Werf, P. P., & Israel, F. P. 2013, *A&A*, **550**, A12  
 Rovilos, E., Diamond, P. J., Lonsdale, C. J., et al. 2005, *MNRAS*, **359**, 827  
 Ryder, S., Covarrubias, R., Amy, S., et al. 2010a, *CBET*, **2242**, 1  
 Ryder, S. D., Amy, S. W., Stockdale, C. J., et al. 2010b, *ATel*, **2450**, 1  
 Ryder, S. D., Amy, S. W., Stockdale, C. J., et al. 2011a, *ATel*, **3370**, 1  
 Ryder, S. D., Sadler, E. M., Subrahmanyam, R., et al. 2004, *MNRAS*, **349**, 1093  
 Ryder, S. D., Stockdale, C. J., Immler, S., et al. 2011b, *ATel*, **3764**, 1  
 Salas, P., Bauer, F. E., Stockdale, C., & Prieto, J. L. 2013, *MNRAS*, **428**, 1207  
 Shepherd, M. C. 1997, in ASP Conf. Ser. 125, Astronomical Data Analysis Software and Systems VI, ed. G. Hunt & H. Payne (San Francisco, CA: ASP), 77  
 Soderberg, A. M., Berger, E., Page, K. L., et al. 2008, *Natur*, **453**, 469  
 Soderberg, A. M., Brunthaler, A., Nakar, E., Chevalier, R. A., & Bietenholz, M. F. 2010, *ApJ*, **725**, 922  
 Soderberg, A. M., Chevalier, R. A., Kulkarni, S. R., & Frail, D. A. 2006a, *ApJ*, **651**, 1005  
 Soderberg, A. M., Kulkarni, S. R., Berger, E., et al. 2005, *ApJ*, **621**, 908  
 Soderberg, A. M., Nakar, E., Berger, E., & Kulkarni, S. R. 2006b, *ApJ*, **638**, 930  
 Sramek, R. A., Panagia, N., & Weiler, K. W. 1984, *ApJL*, **285**, L59  
 Stockdale, C. J., Kelley, M., van Dyk, S. D., et al. 2005, *IAU Circ.*, **8603**, 2  
 Stockdale, C. J., Williams, C. L., Weiler, K. W., et al. 2007, *ApJ*, **671**, 689  
 Takano, S., Hofner, P., Winnewisser, G., Nakai, N., & Kawaguchi, K. 2005, *PASJ*, **57**, 549  
 Tingay, S. J. 2004, *AJ*, **127**, 10  
 Turner, J. L., & Ho, P. T. P. 1985, *ApJL*, **299**, L77  
 Ulvestad, J. S. 2009, *AJ*, **138**, 1529  
 Ulvestad, J. S., & Antonucci, R. R. J. 1991, *AJ*, **102**, 875  
 Ulvestad, J. S., & Antonucci, R. R. J. 1994, *ApJL*, **424**, L29  
 Ulvestad, J. S., & Antonucci, R. R. J. 1997, *ApJ*, **488**, 621  
 van Dyk, S. D., Montes, M. J., Weiler, K. W., Sramek, R. A., & Panagia, N. 1998, *AJ*, **115**, 1103  
 van Dyk, S. D., Sramek, R. A., Weiler, K. W., & Panagia, N. 1993, *ApJ*, **409**, 162  
 Weedman, D. W. 1987, in NASA Conference Publication 2466, Star Formation in Galaxies, ed. C. J. Lonsdale Persson (Washington DC: NASA), 351  
 Weiler, K. W., Panagia, N., Montes, M. J., & Sramek, R. A. 2002, *ARA&A*, **40**, 387  
 Weiler, K. W., Panagia, N., Sramek, R. A., et al. 1989, *ApJ*, **336**, 421  
 Weiler, K. W., Panagia, N., Stockdale, C., et al. 2011, *ApJ*, **740**, 79  
 Weiler, K. W., Sramek, R. A., Panagia, N., van der Hulst, J. M., & Salvati, M. 1986, *ApJ*, **301**, 790  
 Weiler, K. W., Williams, C. L., Panagia, N., et al. 2007, *ApJ*, **671**, 1959  
 Wellons, S., Soderberg, A. M., & Chevalier, R. A. 2012, *ApJ*, **752**, 1  
 Williams, C. L., Panagia, N., Van Dyk, S. D., et al. 2002, *ApJ*, **581**, 396  
 Woltjer, L. 1972, *ARA&A*, **10**, 129